

1 Quantifying energy and water fluxes in dry dune ecosystems of the Netherlands

2

3 B.R. Voortman¹, R.P. Bartholomeus¹, S.E.A.T.M. van der Zee², M.F.P. Bierkens^{3,4}, J.P.M.
4 Witte^{1,5}

5

6 [1] KWR Watercycle Research Institute, P.O. Box 1072, 3430 BB Nieuwegein, the
7 Netherlands

8 [2] Soil Physics and Land Management, Environmental Sciences Group, Wageningen
9 University, P.O. Box 47, 6700 AA Wageningen, the Netherlands

10 [3] Department of Physical Geography, Faculty of Geosciences, Utrecht University, P.O. Box
11 80115, 3508 TC Utrecht, the Netherlands

12 [4] Deltares, P.O. Box 85467, 3508 AL Utrecht, the Netherlands

13 [5] VU University, Institute of Ecological Science, Department of Systems Ecology, de
14 Boelelaan 1085, 1081 HV Amsterdam, the Netherlands

15

16 Correspondence to: bernard.voortman@kwrwater.nl

17

18 Keywords: evapotranspiration, dune, moss, heather, longwave radiation, lysimeter, energy
19 balance, the Netherlands

20 **Abstract**

21 Coastal and inland dunes provide various ecosystem services that are related to groundwater,
22 such as drinking water production and biodiversity. To manage groundwater in a sustainable
23 manner, knowledge of actual evapotranspiration (ET_a) for the various land covers in dunes is
24 essential. Aiming at improving the parameterization of dune vegetation in hydro-
25 meteorological models, this study explores the magnitude of energy and water fluxes in an
26 inland dune ecosystem in the Netherlands. Hydro-meteorological measurements were used to
27 parameterize the Penman-Monteith evapotranspiration model for four different surfaces: bare
28 sand, moss, grass and heather. We found that the net longwave radiation (R_{nl}) was the largest
29 energy flux for most surfaces during daytime. However, modelling this flux by a calibrated
30 FAO-56 R_{nl} model for each surface and for hourly time steps was unsuccessful. Our R_{nl}
31 model, with a novel sub-model using solar elevation angle and air temperature to describe the
32 diurnal pattern in radiative surface temperature, improved R_{nl} simulations considerably.
33 Model simulations of evaporation from moss surfaces showed that the modulating effect of
34 mosses on the water balance is species dependent. We demonstrate that dense moss carpets
35 (*Campylopus introflexus*) evaporate more (5%, +14 mm) than bare sand (total of 258 mm in
36 2013), while more open structured mosses (*Hypnum cupressiforme*) evaporate less (-30%, -76
37 mm) than bare sand. Additionally, we found that a drought event in the summer of 2013
38 showed a pronounced delayed signal on lysimeter measurements of ET_a for the grass and
39 heather surfaces respectively. Due to the desiccation of leaves after the drought event, and
40 their feedback on the ~~parameters of the Penman-Monteith equation~~ surface resistance, the
41 potential evapotranspiration in the year 2013 dropped with 9 % (-37 mm) and 10 % (-61 mm)
42 for the grass and heather surfaces respectively, which subsequently led to lowered ET_a of 8 %
43 (-29 mm) and 7 % (-29 mm). These feedbacks are of importance to water resources,
44 especially during a changing climate with increasing number of drought days. Therefore, such
45 feedbacks need to be integrated into a coupled plant physiological and hydro-meteorological
46 model to accurately simulate ET_a . In addition, our study showed that groundwater recharge in
47 dunes can be increased considerably by promoting moss vegetation, especially of open
48 structured moss species.

50 **1 Introduction**

51
52 Coastal and inland sand dunes are major drinking water production sites in the Netherlands.
53 Approximately 23% of Dutch drinking water originates from aquifers in these dunes, which

54 are replenished by both natural groundwater recharge and artificial infiltration of surface
55 waters. Another ecosystem service of groundwater in dune systems is that shallow
56 groundwater tables sustain nature targets with a very high conservation value. Such targets,
57 like wet dune slacks and oligotrophic pools, are often legally enforced, e.g. by the European
58 Habitat Directive and by the Water Framework Directive. Furthermore, a deep layer of fresh
59 groundwater in coastal dunes protects the hinterland from the inflow of saline groundwater.

60 Under a warming climate, summers are expected to become dryer and the water
61 quality of surface waters may degrade (Delpla et al., 2009), especially during dry periods with
62 low river discharge rates (Zwolsman and van Bokhoven, 2007; van Vliet and Zwolsman,
63 2008). To maintain current drinking water quality and production costs, water production in
64 the future may have to rely more on natural groundwater recharge. This implies that drinking
65 water companies need to search for new water production sites or intensify current
66 groundwater extractions, while protecting groundwater dependent nature targets.

67 For sustainable management of renewable groundwater resources, groundwater
68 extractions should be balanced with the amount of precipitation that percolates to the
69 saturated zone, the groundwater recharge. Knowledge of actual evapotranspiration (ET_a , here
70 defined as the sum of plant transpiration, soil evaporation, and evaporation from canopy
71 interception) for the various land covers is essential to quantify the amount of recharge. Inland
72 dune systems are predominantly covered with deciduous and pine forest. Well-developed
73 hydro-meteorological models are available to simulate ET_a for these forest ecosystems
74 (Dolman, 1987; Moors, 2012). Other ecosystems, such as heathland and bare sand colonized
75 by algae, mosses, tussock forming grasses or lichens, received less attention. However,
76 heathland and drift sand ecosystems have a higher conservation value than forest plantations,
77 in particular of coniferous trees. Nature managers are therefore often obligated to protect and
78 develop certain heathland and drift sand ecosystems at the expense of forest ecosystems (The
79 European Natura 2000 policy). A better parameterization of heathland and drift sand
80 ecosystems in hydro-meteorological models would aid in the sustainable management of
81 important groundwater resources and would allow quantifying the cost and benefit of nature
82 conservation in terms of groundwater recharge.

83 To this end, this study explores diurnal patterns in energy and water fluxes in a dry
84 dune ecosystem on an elevated sandy soil in the Netherlands. Our study aims at improving the
85 parameterization of dune vegetation in hydro-meteorological models based on field
86 measurements, focusing on four different surfaces: bare sand, moss (*Campylopus introflexus*),
87 grass (*Agrostis vinealis*) and heather (*Calluna vulgaris*). A second objective is to quantify the

88 effect of moss species on the water balance. Mosses and lichens are present in most
89 successional stages in dry dune ecosystems, either as pioneer species or as understory
90 vegetation. Voortman et al. (2013) hypothesized that moss covered soils could evaporate less
91 than a bare soil, since the unsaturated hydraulic properties of moss layers reduce temper
92 evaporation under relatively moist conditions. Such hydraulic behavior could have large
93 implications on the ecological interactions between vascular and nonvascular plants in water
94 limited ecosystems, as the presence of a moss cover could facilitate the water availability for
95 rooting plants. Such interactions are of importance to groundwater resources as the resilience
96 of plant communities to drought determines the succession rate and biomass, which
97 subsequently feedback on evapotranspiration.

98 A third objective is to get insight in the delayed effect of dry spells on potential and
99 actual evapotranspiration for heathlands and grasslands. To quantify the evapotranspiration
100 loss term, many hydrological modeling frameworks use the concept of potential
101 evapotranspiration ET_p (Federer et al., 1996; Kay et al., 2013; Zhou et al., 2006), defined as the
102 maximum rate of evapotranspiration from a surface where water is not a limiting factor
103 (Shuttleworth, 2007). ET_p is input to modeling frameworks and reduces to ET_a in cases of
104 water stress. However, if dry spells result in a vegetation dieback, the simulated ET_p should be
105 adjusted to account for the smaller transpiring leaf area after the dry spell. The model
106 simulations presented in this paper give some guidance on the magnitude of errors in
107 simulated ET_a if feedbacks of dry spells on ET_p are neglected.

108 The knowledge presented in this paper will help to improve and interpret the
109 simulations of water recharge in sand dunes by hydrological models, and will sustain
110 rainwater harvesting in dunes by vegetation management.

111

112 **2 Measurements and Methods**

113

114 **2.1 General setup**

115 A field campaign started in August 2012 to measure energy and water fluxes in the drinking
116 water supply area “Soestduinen”, situated on an elevated sandy soil (an ice-pushed ridge) in
117 the center of the Netherlands (52.14° latitude, 5.31° longitude). Due to deep groundwater
118 levels, the vegetation in this region is groundwater-independent, i.e. relying solely on
119 rainwater (on average 822 mm rain per year, 40% falling in the first 6 months of the year and
120 60% falling in the last 6 months of the year). The reference evapotranspiration according to
121 Makkink (1957) is on average 561 mm per year. The field data was used to parameterize the

122 Penman-Monteith equation, to calculate ET_p , and to perform hydrological model simulations
123 of ET_a , based on the actual availability of soil moisture. The Penman-Monteith equation is
124 given by:

125

$$ET_p = \frac{\Delta(R_n - G) + \rho_a c_p (e_s - e_a) / r_a}{\left(\Delta + \gamma \left(1 + \frac{r_s}{r_a} \right) \right) \lambda \rho_w}, \quad 1$$

127

128 where ET_p is the potential evapotranspiration [mm/s], Δ is the slope of the saturation vapor
129 pressure vs. temperature curve [kPa °C⁻¹], R_n is the net radiation [J m⁻²], G is the soil heat flux
130 [J m⁻²], ρ_a is the air density [kg m⁻³], c_p is specific heat of moist air [J kg⁻¹ °C⁻¹], e_s is the
131 saturation vapor pressure of the air [kPa], e_a is the actual vapor pressure of the air [kPa], r_a is
132 aerodynamic resistance to turbulent heat and vapor transfer [s m⁻¹], γ is the psychrometric
133 constant [kPa °C⁻¹], λ is the latent heat of vaporization [J kg⁻¹], and ρ_w is the density of liquid
134 water [kg m⁻³]. Results of Irmak et al. (2005) suggest that estimates of ET_p on hourly time
135 steps are more accurate than estimates on a daily timescale. Furthermore, Liu et al. (2005)
136 showed that the use of daily input values leads to a systematic overestimation of ET_a ,
137 especially for sandy soils. Hence, energy fluxes in the Penman-Monteith equation are
138 preferably simulated at sub-diurnal timescales. Furthermore, understanding and simulation of
139 plant physiological processes requires knowledge of the diurnal variation of environmental
140 variables (Nozue and Maloof, 2006). Therefore, field data was aggregated to hourly time
141 steps to maintain the diurnal pattern and to analyze our field results at the same time interval
142 as commonly available climate data.

143

144

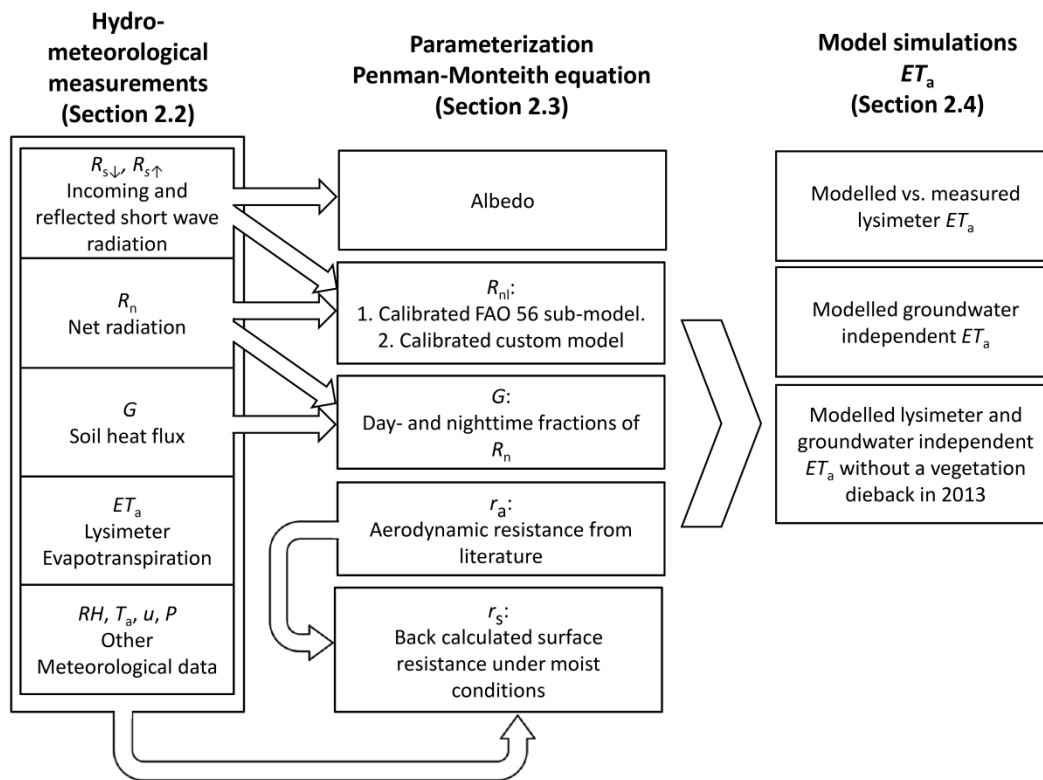
145

146

147

148

In this paper evapotranspiration is defined as the sum of transpiration, soil
evaporation, and evaporation from canopy interception, expressed in mm per time unit.
Radiative and soil heat fluxes are expressed in W m⁻². Fig. 1 shows the procedures followed
to translate field data (section 2.1) to sub-models of the Penman-Monteith equation (section.
2.2) and to subsequently calculate ET_p and simulate ET_a (section 2.3).



149

150 Fig. 1. Organization of the research from measurements to model simulations.

151

152 2.2 Hydro-meteorological measurements

153 Four homogeneous sites of bare sand, moss (*Campylopus introflexus*), grass (*Agrostis*
 154 *vinealis*) and heather (*Calluna vulgaris*) (Fig. 2) were selected to measure actual
 155 evapotranspiration (ET_a), the net radiation (R_n), the soil heat flux (G) and the albedo. Other
 156 meteorological variables such as wind speed (u , at 2 m above the surface), relative humidity
 157 (RH , 1.5 m above the surface), air temperature (T_a , 1.5 m above the surface), and rain (P)
 158 were measured at a weather station, installed in-between the measurement plots at a
 159 maximum distance of 40 m from each plot. Measurements were collected with data loggers
 160 (CR1000, Campbell Scientific Inc.) at a 10 second interval and aggregated to minutely values.
 161 Field measurements of bare sand, moss and grass were collected between August 2012 and
 162 November 2013. The field measurements in the heather vegetation were collected between
 163 June 2013 and November 2013.

164



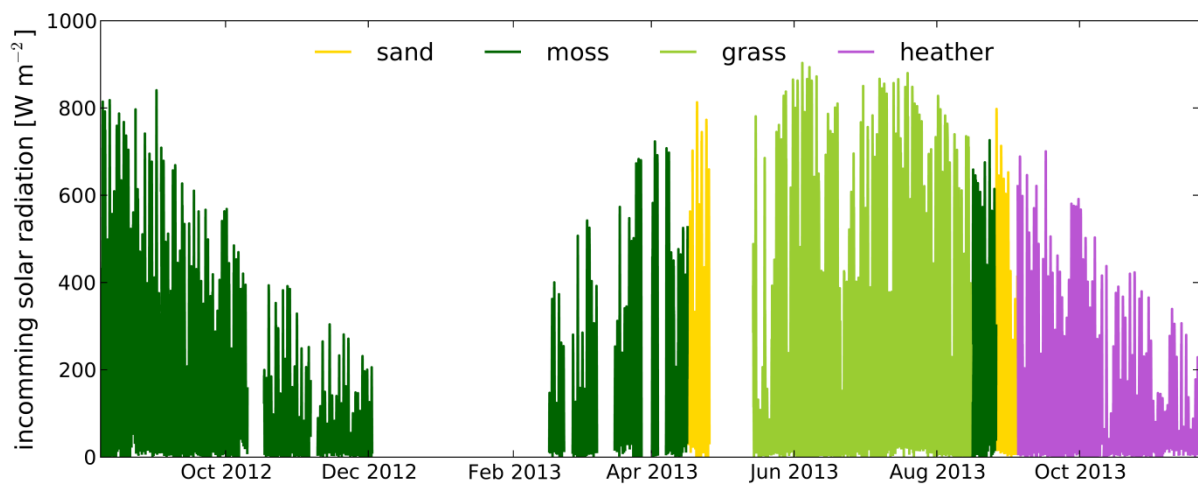
165

166 Fig. 2. The vegetation types studied in this paper, a) the moss surface with an approximately 2
 167 cm thick layer of *Campylopus introflexus* (inset), b) the grass surface, primarily *Agrostis*
 168 *vinealis* and c) the heather surface, *Calluna vulgaris*.
 169

170

170 The net radiation was measured with net radiometers (NRLite2 Kip & Zonen B.V.).
 171 The net radiometers were installed at a relatively low height of 32, 40, 40, and 50 cm above
 172 the bare sand, moss, grass and heather surfaces respectively (relative to the average vegetation
 173 height), to limit the field of view to a homogenous surface. The incoming solar radiation ($R_{s\downarrow}$)
 174 and reflected solar radiation ($R_{s\uparrow}$) were measured with an albedo meter (CMA6, Kip & Zonen
 175 B.V.) that was rotated between the four surfaces. It was installed next to each R_n sensor. Due
 176 to a snow cover (winter months) or sensor maintenance (October 2012, May 2013), some
 177 periods were omitted (Fig. 3).
 178

179



180

180 Fig. 3. Measured incoming solar radiation $R_{s\downarrow}$ at the four different surfaces. Periods with snow
 181 cover or sensor maintenance were omitted.
 182

183

183 Eight self-calibrating heat flux plates (HFP01SC, Hukseflux B.V.) (two for each site)
 184 were installed at 8 cm below the soil surface near the net radiometers. These heat flux plates
 185 were programmed to calibrate themselves for 15 minutes at 6 hour time intervals, based on a
 186 known heat flux supplied by an integrated heater. Besides each soil heat flux plate an

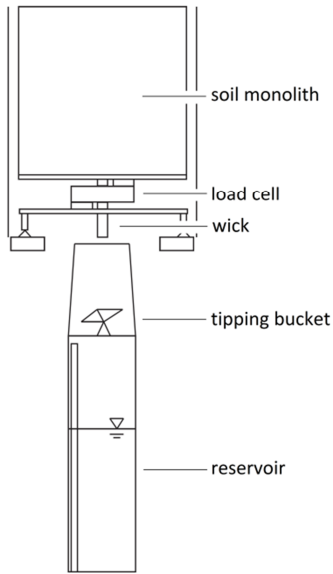
187 averaging thermocouple (TCAV, Campbell Scientific, Inc.) was installed at 2 and 6 cm depth
188 and a soil moisture probe (CS616, Campbell Scientific, Inc) was installed at 4 cm depth~~were~~
189 ~~installed~~ to estimate the change in heat storage (S) above the heat flux plates. The sum of the
190 measured soil heat flux at 8 cm depth and S represents the heat flux at the soil surface. Sensor
191 installation and procedures to calculate S were followed according to the HFP01SC
192 instruction manual of Campbell Scientific Inc. (2014).

193 Within each surface, one weighing lysimeter was installed. The lysimeters (Fig. 4) had
194 a 47.5 cm inner diameter and were 50 cm deep. Intact soil monoliths were sampled by
195 hammering the PVC tube into the soil, alternated with excavating the surrounding soil to
196 offset soil pressures. The lysimeters were turned upside down, to level the soil underneath and
197 to close this surface with a PVC end cap. To allow water to drain out of the lysimeter bottom
198 plate, a 2.5 cm diameter hole was made in the base plate. A 15 cm long fiberglass wick
199 (Pepperell 2 x ½ inch) was installed in the PVC end cap to guide drainage water through the
200 hole into a tipping bucket (Davis 7852) below the lysimeter. The wick, together with two
201 sheets of filter cloth (140-150 μm , Eijkelkamp Agrisearch Equipment), placed at the bottom
202 of the lysimeter tank, prevented soil particles from flushing out of the lysimeter. The tipping
203 bucket below the lysimeter had a resolution of 0.2 mm for the intercepting area of the tipping
204 bucket, which was equal to 0.024 mm for the cross-sectional area of the lysimeter. Drainage
205 water was collected in a reservoir installed below the lysimeter.

206 The lysimeters were weighted with temperature compensated single point load cells
207 (Utilcell 190i, max 200 kg). These load cells were initially connected to the full bridge data
208 ports of the data loggers. However, the measurement resolution of the data loggers was too
209 coarse to fully compensate for temperature effects on weight measurements. Fluctuations of
210 0.333 μV due to temperature effects were within the data logger measurement resolution,
211 which equals 36 g in weight change, i.e. 0.2 mm of evaporation. To increase the lysimeter
212 precision, digitizers (Flintec LDU 68.1) were installed in May 2013 to process and digitize the
213 load cell signals without interference of the data logger. In this setup, a measurement
214 resolution of 10 g was achieved, i.e. 0.06 mm equivalent water depth, which is adequate for
215 measuring ET_a for daily time periods (subtracting two values would lead to a maximum error
216 of 0.06 mm caused by the measurement resolution). Analysis of measured ET_a were therefore
217 limited to the period after installation of the digitizers.

218 After a rain event on September 7 2013, the tipping buckets below the grass and
219 heather lysimeters became partly clogged with beetles nesting underneath the lysimeters. This
220 led to a continuous drainage signal which was out of phase with the weight measurements.

221 Without accurate drainage measurements, lysimeter weight signals cannot be transferred to
 222 evapotranspiration. Therefore, ET_a data on days with a poor drainage signal after September 7
 223 2013 were disregarded in the analyses for the grass and heather lysimeters.



224
 225 Fig. 4. Lysimeter design.
 226

227 2.3 Parameterization of the Penman-Monteith equation

228 2.3.1 Net radiation (R_n)

229 The net radiation (R_n) is defined as:

230

$$231 \quad R_n = R_{ns} + R_{nl} = (1 - \text{albedo})R_{s\downarrow} + (\varepsilon_s R_{l\downarrow} - R_{l\uparrow}), \quad 2$$

232

233 where R_{ns} is the net shortwave radiation, R_{nl} is the net longwave radiation, $R_{s\downarrow}$ is the incoming
 234 solar radiation, $R_{l\downarrow}$ is the downwelling longwave radiation from the atmosphere to the surface,
 235 $R_{l\uparrow}$ is the emitted longwave radiation by the surface into the atmosphere and ε_s is the surface
 236 emissivity representing the reflected downwelling longwave radiation. The albedo in Eq. 2
 237 was determined by linear regression between measured $R_{s\downarrow}$ and $R_{s\uparrow}$. Based on the albedo
 238 obtained this way, R_{nl} follows from measurements of R_n by subtracting calculated R_{ns} from
 239 measured R_n . Throughout this paper, this back-calculated R_{nl} is referred to as the measured
 240 R_{nl} .

241 In hydro-meteorological models, R_{nl} is commonly estimated under clear sky
 242 conditions and multiplied by a factor to correct for clouds (Irmak et al., 2010;Gubler et al.,
 243 2012;Blonquist Jr et al., 2010;Temesgen et al., 2007). A similar approach was followed in this
 244 study in which the Stefan-Boltzmann law is substituted into Eq. 2 for $R_{l\downarrow}$ and $R_{l\uparrow}$ under clear

245 sky conditions (Saito and Šimůnek, 2009; Van Bavel and Hillel, 1976) and multiplied by a
 246 cloudiness function to obtain R_{nl} :

247

$$248 \quad R_{nl} = (\varepsilon_s \varepsilon_a \sigma T_a^4 - \varepsilon_s \sigma T_s^4) f_{cd}, \quad 3$$

249

250 where ε_a is the clear sky emissivity of the atmosphere [-], ε_s is the surface emissivity [-], σ is
 251 the Stefan-Boltzmann constant ($5.67 \times 10^{-8} \text{ W m}^{-2} \text{ K}^{-1}$), T_a is the air temperature [K], T_s is the
 252 surface temperature [K] and f_{cd} is a cloudiness function [-] (described later). For vegetated
 253 surfaces $\varepsilon_s = 0.95$ was used (based on Jones (2004)), and $\varepsilon_s = 0.925$ for bare sand (based on
 254 Fuchs and Tanner (1968)). Estimating ε_a has a long history and numerous parameterizations
 255 are available. In this study the empirical relationship found by Brunt (1932) was used:

256

$$257 \quad \varepsilon_a = 0.52 + 0.065 \sqrt{e_a}, \quad 4$$

258

259 where e_a is the water vapor pressure measured at screen level [hPa]. The cloudiness function
 260 f_{cd} in Eq. 3 is limited to $0.05 \leq f_{cd} \leq 1$ and equal to:

261

$$262 \quad f_{cd} = \frac{R_{s\downarrow}}{R_{s0}}, \quad 5$$

263

264 where R_{s0} is the estimated clear sky solar radiation. We estimated R_{s0} following the FAO
 265 irrigation and drainage paper No. 56 (Allen et al., 1998). Since f_{cd} is undefined during the
 266 night, an interpolation of f_{cd} between sunset and sunrise is required. According to Gubler et al.
 267 (2012) f_{cd} can be best linearly interpolated between the four to six hour average before sunset
 268 and after sunrise. We adopted this approach, applying a five-hour average.

269 | An estimate of T_s is required to fully parameterize Eq. 3. We ~~have chosen to develop~~
 270 use a new approach to simulate the diurnal pattern in T_s . Using Eq. 3, we back-calculated $T_s -$
 271 T_a based on measured R_{nl} for clear hours ($f_{cd} > 0.9$). Generally, $T_s - T_a$ will be negative during
 272 nighttime (when solar elevation β [radians] < 0), and will gradually increase to positive values
 273 during daytime ($\beta > 0$). We describe this pattern by (Fig. 5):

274

$$275 \quad T_s - T_a = f_{cum}(\beta, \mu_\beta, \sigma_\beta) [T_{s,amp} + \beta T_{s,slope}] + T_{s,offset}, \quad 6$$

276

277 where f_{cum} is a cumulative normal distribution function with mean μ_β and standard deviation
 278 σ_β , describing the moment at which the surface becomes warmer than the air temperature (μ_β)
 279 and the speed at which the surface warms up or cools down (σ_β) as a function of solar
 280 elevation angle (β). $T_{s,\text{amp}}$ is the amplitude of T_s [K], $T_{s,\text{slope}}$ is the slope between β and $T_s - T_a$
 281 during daytime [K/radians] and $T_{s,\text{offset}}$ is the average value of $T_s - T_a$ during nighttime [K].
 282 The parameters of Eq. 6, except $T_{s,\text{offset}}$, were fitted to the data by minimizing the root mean
 283 squared error (*RMSE*) by generalized reduced gradient nonlinear optimization. The $T_{s,\text{offset}}$ was
 284 determined as the average nighttime $T_s - T_a$ to limit the amount of parameters during the
 285 optimization. Equation 6 was substituted for T_s in Eq. 3 to estimate R_{nl} . This novel approach
 286 to derive R_{nl} was compared to the R_{nl} model of the FAO-56 approach (Allen et al., 1998),
 287 originally derived to obtain daily estimates of R_{nl} (using minimum and maximum daily T_a
 288 divided by 2 instead of T_a in Eq. 7) but commonly applied at hourly timescales (ASCE-EWRI,
 289 2005;Perera et al., 2015;Gavilán et al., 2008;López-Urrea et al., 2006):

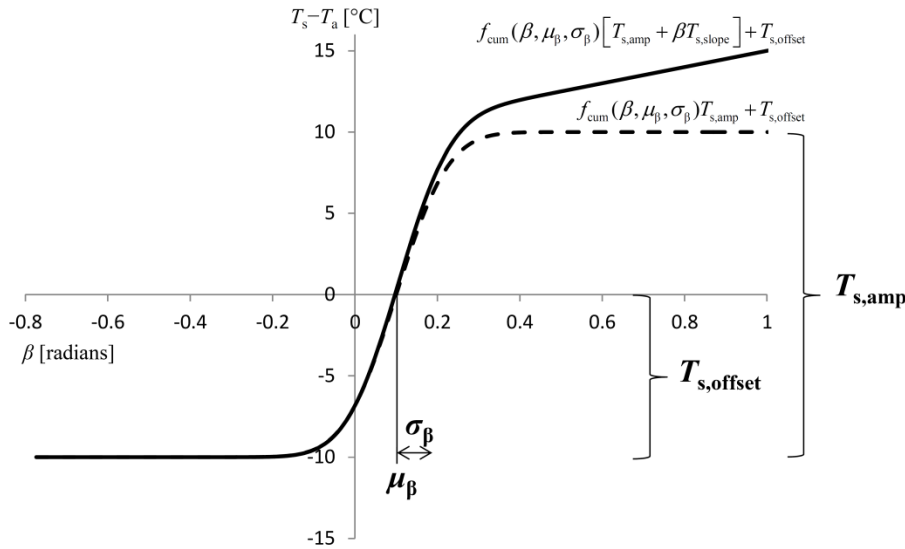
290

$$291 \quad R_{\text{nl}} = -\sigma T_a^4 \left(a - b \sqrt{e_a} \right) \left(1.35 \frac{R_s}{R_{s0}} - 0.35 \right), \quad 7$$

292

293 where the first term between brackets represents the net emittance, which should compensate
 294 for the fact that T_s is not measured. The empirical parameters a en b can be calibrated for a
 295 specific climate and/or vegetation. The second term between brackets is a cloudiness function.
 296 The default parameter values for a and b are 0.34 and 0.14, respectively (Allen et al., 1998).
 297 We calibrated these parameters for every site by linear least squares regression for clear days
 298 ($R_s/R_{s0} > 0.9$) and compared the performance of both R_{nl} models (Eq. 3 and Eq. 7).

299



300

301 Fig. 5. Eq. 6 and associated parameters to describe the surface-air temperature difference,
 302 substituted for T_s in R_{nl} (Eq. 3).

303

304 2.3.2 Soil heat flux (G)

305 The soil heat flux is commonly expressed as a fraction of R_n , particularly at large scales using
 306 remote sensing (Su, 2002; Bastiaanssen et al., 1998; Kustas et al., 1998; Kustas and Daughtry,
 307 1990; Friedl, 1996). We adopted the same approach making a distinction between daytime
 308 (F_{day}) and nighttime (F_{night}) fractions, determined by linear least squares regression between
 309 R_n and the average of the two sets of soil heat flux measurements.

310

311 2.3.3 Aerodynamic resistance (r_a)

312 The aerodynamic resistance under neutral stability conditions can be estimated by (Monteith
 313 and Unsworth, 1990):

314

$$r_a = \frac{\ln \left[\frac{z_m - d}{z_{om}} \right] \ln \left[\frac{z_h - d}{z_{oh}} \right]}{k^2 u_z},$$

315

8

316

317 where z_m is the height of wind speed measurements [m], d is the zero plane displacement
 318 height [m], z_{om} is the roughness length governing momentum transfer [m], z_h is the height of
 319 the humidity measurements [m], z_{oh} is the roughness length governing transfer of heat and
 320 vapor [m], k is the von Karman's constant (0.41 [-]) and u_z is the wind speed at height z_m
 321 [m/s]. For grass, empirical equations are developed (FAO 56 approach) to estimate d , z_{om} and
 322 z_{oh} :

323

324 $d = 0.66V,$ 9

325 $z_{om} = 0.123V,$ 10

326 $z_{oh} = 0.1z_{om},$ 11

327

328 where V is the vegetation height. Wallace et al. (1984) found comparable coefficients for
 329 heather: $d = 0.63V$ and $z_{om} = 0.13V$ and therefore Eq. 9 to 11 were applied for both surfaces
 330 using a constant vegetation height of 7 and 31 cm for the grass and heather surfaces
 331 respectively. For the moss surface, we used a vegetation height of 2 cm, which is equal to the
 332 thickness of the moss mat. For the bare sand surface we assumed $d = 0$ m, and used typical
 333 surface roughness values published by Oke (1978): $z_{oh} = 0.001$ m and $z_{om} = z_{oh}$.

334

335 **2.3.4 Surface resistance (r_s) and canopy interception**

336 Canopy interception was simulated as a water storage which needs to be filled before rain
 337 water reaches the soil surface. A maximum storage capacity of 0.50 mm was defined for
 338 heather following the study of Ladekarl et al. (2005). To our knowledge no literature value of
 339 the interception capacity of the specific grass species (*Agrostis vinealis*) is published.
 340 Considering the relatively low vegetation height we assumed a maximum interception
 341 capacity of 0.25 mm.

342 We distinguished wet (r_{swet}) and dry canopy surface resistance (r_s), since interception
 343 water evaporates without the interference of leaf stomata. During canopy interception (i.e. if
 344 the interception store is fully or partly filled) we used a surface resistance of 0 s/m, reducing
 345 Eq.1 to the Penman equation (Penman, 1948; Monteith and Unsworth, 1990). After the canopy
 346 storage is emptied the surface resistance switches to r_s . The r_s was back-calculated for
 347 daytime periods for the heather and grass lysimeters by substituting measured R_n , G , ET_a , e_s
 348 and e_a and simulated r_a into Eq. 1 under non-stressed conditions (i.e. $ET_p = ET_a$). Nighttime
 349 evaporation was assumed to be equal to 0 mm. To make sure that the back-calculated r_s was
 350 based on days at which evapotranspiration occurred at a potential rate, it was back-calculated
 351 for every two consecutive days after precipitation events and after emptying of the
 352 (calculated) interception store. The surface resistance (r_s) of bare sand and moss was assumed
 353 to be equal to 10 s/m, i.e. similar to the surface resistance under well watered conditions of
 354 bare soil found by Van de Griend and Owe (1994).

355 During the summer of 2013, a dry spell (from 4-7-2013 until 25-7-2013) resulted in a
356 vegetation dieback of grass and heather. Surface resistances were back-calculated for periods
357 before and after the drought event. The drought event had 22 consecutive dry days with a
358 cumulative reference evapotranspiration according to Makkink (1957) of 85 mm. Drought
359 events of similar magnitude have been recorded 12 times during the past 57 years (from 1958
360 until 2014) at climate station “de Bilt” located in the center of the Netherlands (52.1° latitude,
361 5.18° longitude), 10 km from the measurement site. The measurements in the heather
362 vegetation started a week before the drought event. During this week, there were two days
363 (30-6-2013 and 1-7-2013) for which r_s could be back-calculated. The estimated r_s for these
364 days were 35 s m^{-1} and 107 s m^{-1} respectively. We selected the r_s value of the second day to
365 use in our model simulations (107 s m^{-1}) because it was in close agreement with the median
366 surface resistance found by Miranda et al. (1984) of 110 s m^{-1} in a comparable heather
367 vegetation. After the drought event, r_s increased to 331 s m^{-1} ($N = 14$, standard error = 102 s
368 m^{-1}). For the grass vegetation the surface resistance before the drought event was 181 s m^{-1} (N
369 = 9, standard error = 68 s m^{-1}). After the drought event the surface resistance increased to 351
370 s m^{-1} ($N = 4$, standard error = 47 s m^{-1}). Since mosses of these habitats are desiccation tolerant
371 and quickly rehydrate after drought (Proctor et al., 2007), we didn't assess the effect of the
372 dry spell on the surface resistance of the moss surface.

373 The parameters thus obtained were used to parameterize the Penman-Monteith
374 equation and to calculate hourly ET_p values for each surface.

375

376 **2.4 Model simulations of ET_a**

377 Using hourly ET_p of the year 2013 (876 mm precipitation), we used Hydrus 1D (Šimůnek et
378 al., 2008) to simulate ET_a . If meteorological data of the local weather station was missing due
379 to snow cover or sensor maintenance, the meteorological data of weather station “de Bilt” was
380 used (~~10 km from the measurement site~~) for the calculation of ET_p .

381 First, we simulated ET_a for the lysimeter surfaces and compared our results with the
382 lysimeter measurements of ET_a . The lower boundary condition in the model was a seepage
383 face with hydraulic pressure equal to 0 at a depth of 65 cm below the surface (50 cm soil and
384 15 cm wick). Second, we simulated ET_a for the groundwater-independent surroundings. We
385 expected that the availability of soil moisture in the lysimeter tanks was larger than in the
386 groundwater independent surroundings, because the lowest sections of the lysimeters need to
387 be saturated before drainage occurs. To estimate the yearly ET_a of dune vegetation in
388 environments with deep groundwater levels, we used a free drainage boundary condition (i.e.

389 gravity drainage) located 2.5 m below the surface. Third, we investigated the magnitude of the
390 vegetation dieback in the summer of 2013 on both ET_p and ET_a , by using two different surface
391 resistances: one derived from the period before, and one for the period after the vegetation
392 dieback.

393 Soil hydraulic properties in the hydrological model were described by the Van
394 Genuchten relationships (Van Genuchten, 1980). Soil samples (100 cm^3) collected next to
395 each lysimeter at 5 and 15 cm depth were used to derive the drying retention function. The
396 average drying retention parameters (of the two samples collected next to each lysimeter)
397 were used in the hydrological model taking hysteresis into account by assuming the wetting
398 retention curve parameter (α_{wet}) to be twice as large as the drying retention curve parameter
399 (α_{dry}) (Šimůnek et al., 1999). The unsaturated hydraulic properties (parameters l and K_0) were
400 estimated using the Rosetta database and pedotransfer functions, providing the fitted drying
401 retention curve parameters as input (Schaap et al., 2001). The hydraulic properties of the 15
402 cm long wick, guiding drainage water below the lysimeter into the tipping bucket, were taken
403 from Knutson and Selker (1994).

404 Since mosses have neither leaf stomata nor roots, ET_a from the moss surface is limited
405 by the capacity of the moss material to conduct water to the surface. This passive evaporation
406 process is similar to the process of soil evaporation, i.e. evaporation becomes limited if the
407 surface becomes too dry to deliver the potential rate. The unsaturated hydraulic properties of
408 the dense *Campylopus introflexus* moss mat covering the lysimeter soil were based on the
409 hydraulic properties derived by Voortman et al. (2013) and used in the first 2 cm of the model
410 domain. Macro pores in the moss mat were neglected by Voortman et al. (2013), which
411 implies that direct implementation of these hydraulic properties would result in large amounts
412 of surface runoff generation or ponding, since the unsaturated hydraulic conductivity (K_0) of
413 the moss mat is lower than 0.28 cm/d. Therefore, the dual porosity model of Durner (1994)
414 was used to add 1000 cm/d to the hydraulic conductivity curve of Voortman et al. (2013)
415 between -1 and 0 cm pressure head (Appendix A). This permits the infiltration of rain water at
416 high intensity rain showers without affecting the unsaturated hydraulic behavior at negative
417 pressure heads. Because of the complex shape of the retention function of the moss mat,
418 hysteresis in the soil hydraulic functions in the underlying soil was neglected for the
419 simulation of evaporation from moss surfaces. The sensitivity of this simplification on the
420 model outcomes was investigated by adjusting the soil hydraulic function of the soil from the
421 drying to the wetting curve. This had a negligible effect (<1 mm) on the simulated yearly ET_a
422 (data not shown). Besides simulations of moss evaporation with a cover of *Campylopus*

423 *introflexus*, soil physical characteristics of *Hypnum cupressiforme* were used in the first 2 cm
424 of the model domain to analyze the effect of different moss species on the water balance. Soil
425 parameters used in the model are explained in more detail in Appendix A.

426 Since the grass and heather lysimeters fully covered the soil, soil evaporation was
427 neglected for these surfaces. The root profile for the grass and heather lysimeters was 30 cm
428 deep, with the highest concentration of roots in the upper layer decreasing linearly with depth.
429 A water stress reduction function (Feddes et al., 1978) was used to simulate the closure of leaf
430 stomata during water stressed periods. Vegetation parameters are explained in more detail in
431 Appendix B. Modeled actual evapotranspiration ($ET_{a,mod}$) was aggregated to daily values and
432 compared to field measurements of ET_a during moist ($ET_{a,mod} = ET_p$) and dry conditions ($ET_{a,mod} \neq ET_p$).
433

434

435 **2.5 Model performance assessment**

436 Model performance of R_{ns} , R_{nl} , G and $ET_{a,mod}$ simulations were tested with the Nash-Sutcliffe
437 model efficiency coefficient (NSE):

438

$$439 \quad NSE = 1 - \frac{\sum_{t=1}^N (x_{o,t} - x_{m,t})^2}{\sum_{t=1}^N (x_{o,t} - \bar{x}_o)^2}, \quad 12$$

440

441 Where N is the total number of observations, $x_{m,t}$ is the model-simulated value at time step t ,
442 $x_{o,t}$ is the observed value at time step t , and \bar{x} is the mean of the observations. $NSE = 1$
443 corresponds to a perfect match of modeled to observed data. If $NSE < 0$, the observed mean is
444 a better predictor than the model. To assess the magnitude of error of model simulations, the
445 root mean squared error ($RMSE$), the mean difference (MD) and the mean percentage
446 difference ($M\%D$) were used.

447

448 **3 Results and Discussion**

449

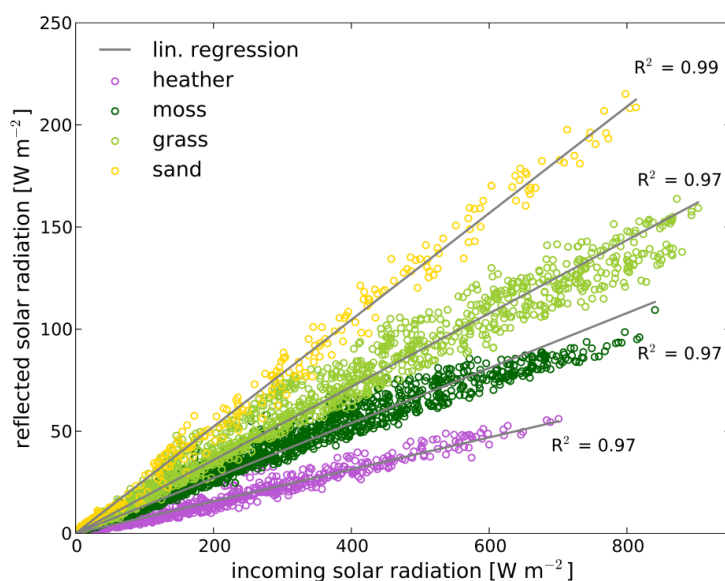
450 **3.1 Parameterization of the Penman-Monteith equation**

451

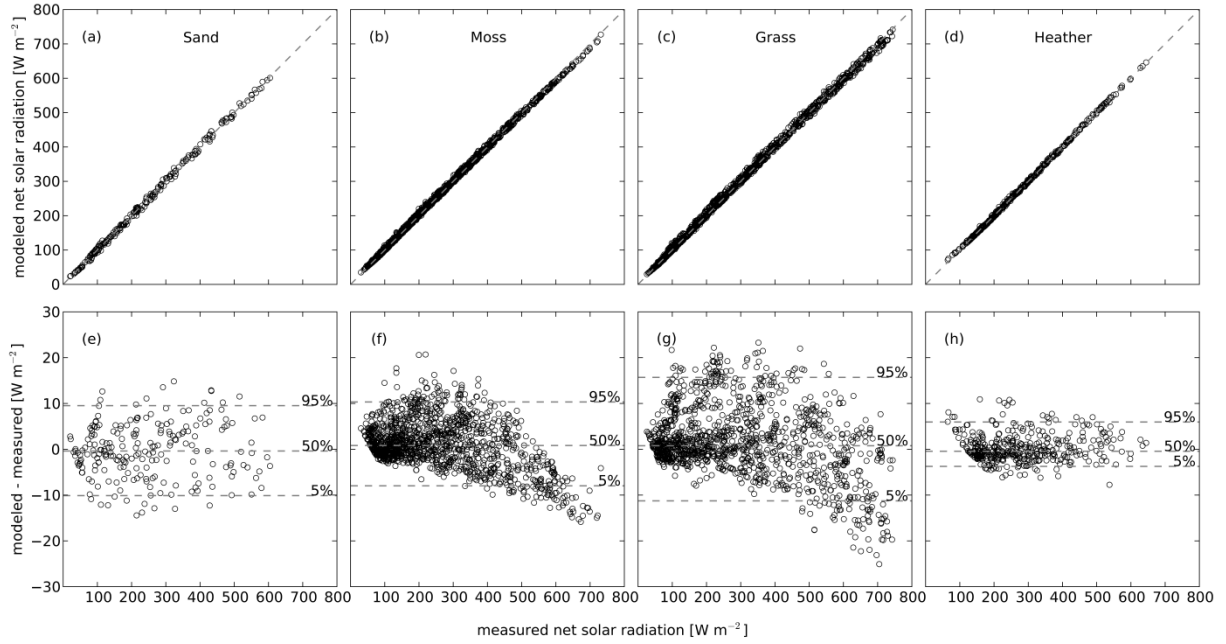
452 **3.1.1 Net shortwave radiation**

453 The measured incoming and reflected solar radiation were used to compute the albedo of the
 454 four surfaces by linear regression (Fig. 6; Table 5). This single value for the albedo slightly
 455 overestimates the reflected solar radiation at large incoming solar radiation (Fig. 7) because of
 456 a dependency of the albedo on solar elevation angle β (Yang et al., 2008; Zhang et al., 2013).
 457 Nonetheless does the use of a single value for the albedo hardly affect the error in modeled
 458 R_{ns} : The mean difference (MD) between measured and modeled R_{ns} lies between -0.23 and
 459 1.63 Wm^{-2} (Table 1), which is equal to the energy required to evaporate 0.008 to 0.057 mm d⁻¹.
 460 The NSE for estimating R_{ns} is close to 1 (Table 1), showing almost a perfect match of
 461 modeled to observed data.

462 The dense moss mat *Campylopus introflexus* entirely covers the underlying mineral
 463 soil, which results in a low albedo (0.135) due to the dark green surface. The albedo of bare
 464 sand (0.261) is comparable to values found in literature for bare dry coarse soils (Qiu et al.,
 465 1998; Van Bavel and Hillel, 1976; Linacre, 1969; Liakatas et al., 1986) and the albedo for grass
 466 (0.179) is consistent with values reported in other studies during summer time (Hollinger et
 467 al., 2010) or for dried grass (Van Wijk and Scholte Ubing, 1963). Heather has a somewhat
 468 lower albedo (0.078) than was found in the literature: Miranda et al. (1984) report an albedo
 469 of 0.13 (*Calluna*, LAI ca. 4); Wouters et al. (1980) report an albedo of 0.102 (*Calluna*). The
 470 heather vegetation in our study was in a later successional stage with aging shrubs having a
 471 relatively large fraction of twigs and a smaller LAI (3.47) than found by Miranda et al.
 472 (1984). Furthermore, the albedo data of heather vegetation was collected primarily past the
 473 growing season from September till November. The darker surface after the growing season
 474 and the lower LAI explains the small albedo compared to other studies.



475
 476 Fig. 6. Linear regressions between incoming and reflected solar radiation.



477

478 Fig. 7. Modeled compared to measured net solar radiation (figures a- d, dashed lines are 1:1
 479 lines) and deviations from the 1:1 line (figures e- h, dashed lines indicate 5, 50 and 95
 480 percentiles).

481 Table 1. Model performance of R_{ns} simulations

| Surface | N | NSE | $RMSE$ [Wm ⁻²] | MD [Wm ⁻²] | $M\%D$ [%] |
|---------|------|-------|-------------------------------|-----------------------------|---------------|
| Sand | 218 | 0.998 | 5.99 | -0.23 | -0.10 |
| Moss | 1317 | 0.999 | 5.46 | 1.18 | 0.46 |
| Grass | 1203 | 0.998 | 7.78 | 1.63 | 0.55 |
| Heather | 407 | 0.999 | 3.00 | 0.24 | 0.09 |

482

483 3.1.2 Net longwave radiation

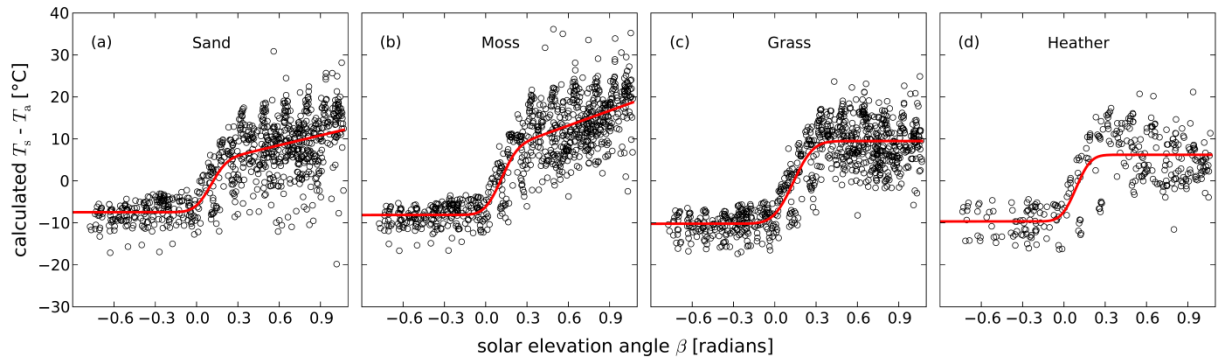
484 The fitted function of Eq. 6 describes the dynamics of the surface temperature relative to air
 485 temperature (Fig. 8; Table 5). All surfaces have a similar average nighttime surface
 486 temperature ($T_{s,offset}$) relative to T_a , ranging between -7.47 and -10.21°C. The solar elevation
 487 angle at which the surfaces become warmer than the air temperature (μ_β), as well as the speed
 488 at which the surface warms up or cools down (σ_β), are comparable between the surfaces. The
 489 main difference between the surfaces is observed at high solar elevation angles. Sand and
 490 moss show a clear increasing slope during the day, while grass and heather are able to
 491 attenuate the increase in surface temperature, possibly due to a larger latent heat flux (Fig. 8).
 492 The moss surface shows the largest increase in surface temperature during the day. Although
 493 organic layers, e.g. dry peat, have a larger specific heat (1600 J kg⁻¹K⁻¹) than dry sand (693 J

494 $\text{kg}^{-1}\text{K}^{-1}$) (Gavriliiev, 2004), the energy required to heat up the moss material is much smaller
495 than for sand, because of the small dry bulk density of ca. 26.8 g/l (derived for *Campylopus*
496 *introflexus* from Voortman et al. (2013)). Therefore, the surface temperature and the emitted
497 longwave radiation are largest for the moss surface.

498 Our R_{nl} model (Eq. 3 and Eq. 6) simulates R_{nl} much better than the calibrated (Table 2)
499 FAO-56 R_{nl} sub-model (Table 3). For the natural grass surface, the *NSE* even becomes
500 negative using the calibrated FAO-56 approach. Several studies showed that the FAO-56 R_{nl}
501 sub-model underestimates the magnitude of R_{nl} for reference grass vegetation and poorly
502 describes the diurnal pattern (Matsui, 2010;Blonquist Jr et al., 2010;Yin et al.,
503 2008;Temesgen et al., 2007). As mentioned, the FAO-56 R_{nl} sub-model was originally
504 developed for reference grass vegetation under well-watered conditions for daily time steps,
505 but is commonly applied at hourly timescales (ASCE-EWRI, 2005;Perera et al., 2015;Gavilán
506 et al., 2008;López-Urrea et al., 2006;Irmak et al., 2005). At daily time steps, T_s is close to T_a ,
507 since the warmer daytime T_s is compensated by the cooler nighttime T_s . For hourly time steps,
508 the assumption that T_s follows T_a is not valid, which explains the poor performance of the
509 FAO-56 R_{nl} model for hourly time steps. This poor performance cannot be compensated by
510 calibrating the net emissivity parameters, since the diurnal pattern remains unaffected.

511 In this analysis a typical pattern in T_s relative to T_a is used to estimate T_s (Eq. 6), and
512 subsequently R_{nl} (Eq. 3). This relationship (Fig. 8) is sensitive to local weather conditions,
513 which implies that the parameters of Eq. 6 (Table 5) are not directly transferable to other
514 locations or climates. The applicability of the presented approach to simulate R_{nl} should be
515 tested before it is used for other surfaces or climates. It should be noted that the amount of
516 parameters that is required to simulate R_{nl} is relatively large. However, μ_{β} as well σ_{β} , are
517 comparable between the surfaces. These parameters might be assumed similar for every
518 surface, reducing the species specific model parameters to three (one more than the FAO-56
519 approach). More data of different vegetation types is required to generalize these results and
520 to assess the amount of parameters that are required to accurately simulate R_{nl} .

521



522

523 Fig. 8. Measured surface temperature relative to air temperature ($T_s - T_a$) for clear hours ($f_{cd} >$
 524 0.9) as function of solar elevation angle β . Relationships (red lines) were fitted to the data
 525 using Eq. 6.

526

527 Table 2. Calibrated net emissivity parameters of the FAO-56 R_{nl} sub-model (Eq. 7).

| | a | b |
|---------|------|-------|
| Sand | 0.31 | -0.00 |
| Moss | 0.33 | 0.02 |
| Grass | 0.36 | -0.06 |
| Heather | 0.24 | 0.02 |

528

529 Table 3. Model performance of R_{nl} simulations for hourly time steps.

| Surface | N | NSE | $RMSE$ [Wm^{-2}] | MD [Wm^{-2}] | $M\%D$ [%] |
|---------------------------|------|-------|-------------------------|-----------------------|---------------|
| Using Eq. 3 | | | | | |
| Sand | 5891 | 0.65 | 27.37 | 0.92 | 1.52 |
| Moss | 5997 | 0.74 | 28.57 | 3.73 | 5.19 |
| Grass | 6113 | 0.71 | 25.66 | 1.41 | 2.36 |
| Heather | 2424 | 0.63 | 27.63 | -0.21 | -0.40 |
| Using FAO-56 Eq. 7 | | | | | |
| Sand | 5891 | 0.41 | 35.39 | 4.34 | 7.14 |
| Moss | 5997 | 0.31 | 46.67 | 14.84 | 20.65 |
| Grass | 6113 | -0.07 | 49.41 | -18.23 | -30.38 |
| Heather | 2424 | 0.29 | 38.24 | 10.50 | 19.54 |

530

531 3.1.3 Soil heat flux

532 The soil heat flux G as fraction of R_n (F_{day} and F_{night}) decreases with vegetation cover (Table
 533 5). The nighttime fractions are larger than the daytime fractions, as R_n becomes smaller in

534 magnitude during the night, which simultaneously corresponds to a change in direction of R_n
 535 and G , from downward (positive) to upward (negative). Relatively small systematic errors are
 536 made using daytime and nighttime fractions of R_n to simulate G (MD between 1.92 and 0.69
 537 W m^{-2}) (Table 4). In remote sensing algorithms G is often simulated as fraction of R_n ,
 538 depending on the LAI or the fractional vegetation cover. In e.g. the SEBS algorithm, the soil
 539 heat flux fraction (F) is interpolated between 0.35 for bare soil and 0.05 for a full vegetation
 540 canopy (Su, 2002). These limits are close to the bare sand (0.270) and heather (0.066) F_{day}
 541 fractions (Table 5). The heather F_{day} (0.066) was close to the value found by Miranda et al.
 542 (1984) of 0.04.

543 The analysis of the relationship between R_n and G was based on the average of two
 544 sets of soil heat flux plates per surface. These sets of measurements showed on average a
 545 good agreement: a MD below 1.07 Wm^{-2} with a $RMSE$ ranging between 5.02 and 9.40 Wm^{-2} .
 546

547 Table 4. Model performance of G simulations.

| Surface | N | NSE | $RMSE$ [Wm^{-2}] | MD [Wm^{-2}] | $M\%D$ [%] |
|----------------|-----------------------|-------------------------|--|--|----------------------------------|
| Sand | 6080 | 0.820 | 20.06 | 1.92 | 22.16 |
| Moss | 5335 | 0.901 | 12.02 | 1.65 | 24.29 |
| Grass | 6046 | 0.868 | 8.97 | 1.60 | 43.42 |
| Heather | 2028 | 0.641 | 11.39 | 0.69 | 40.27 |

548

549

550 Table 5. Parameters of the four different surfaces used for the calculation of ET_p for hourly
 551 time steps.

| Parameter | Sand | Moss | Grass | Heather |
|---|-------------|-------------|--------------|----------------|
| albedo [-] | 0.261 | 0.135 | 0.179 | 0.078 |
| μ_β [radians] | 0.10 | 0.10 | 0.13 | 0.09 |
| σ_β [radians] | 0.09 | 0.09 | 0.11 | 0.08 |
| $T_{s,amp}$ [°C] | 11.26 | 14.21 | 19.70 | 15.89 |
| $T_{s,offset}$ [°C] | -7.47 | -8.14 | -10.21 | -9.67 |
| $T_{s,slope}$ [°C radians ⁻¹] | 7.83 | 11.82 | 0.00 | 0.00 |
| F_{day} [-] | 0.270 | 0.211 | 0.129 | 0.066 |
| F_{night} [-] | 0.761 | 0.647 | 0.527 | 0.462 |
| r_{swet} [s m ⁻¹] | --- | --- | 0 | 0 |
| r_s [s m ⁻¹] before drought | 10 | 10 | 181 | 107 |
| r_s [s m ⁻¹] after drought | 10 | 10 | 351 | 331 |

552

553 3.1.5 Energy balance

554 All the terms in the energy balance can be defined using daily lysimeter measurements of LE
 555 and an estimate of the sensible heat flux (H) as a residual term of the energy balance. For
 556 daytime measurements (between sunrise and sunset), the LE , H , G , $R_{s\uparrow}$ and R_{nl} can be
 557 expressed as fraction of the $R_{s\downarrow}$. Table 6 summarizes the average fraction of $R_{s\downarrow}$ attributed to
 558 these five different energy fluxes during the measurement campaign. The net longwave
 559 radiation is for most surfaces the largest energy flux during daytime (Table 6).

560 The LE of most surfaces is the second largest flux during daytime, which fraction
 561 increases with vegetation cover. Despite the large difference in albedo between bare sand and
 562 moss, the moss surface has only a slightly larger LE fraction than bare sand (Table 6). This is
 563 primarily caused by the larger R_{nl} flux of moss, which compensates the smaller amount of
 564 reflected solar radiation.

565

566 Table 6. Average fractionation of the incoming shortwave radiation ($R_{s\downarrow}$) between different
 567 energy fluxes during daytime.

| Surface | LE | H | G | $R_{s\uparrow}$ | R_{nl} |
|---------|------|------|------|-----------------|----------|
| Sand | 0.22 | 0.13 | 0.10 | 0.26 | 0.28 |
| Moss | 0.24 | 0.17 | 0.09 | 0.14 | 0.36 |
| Grass | 0.27 | 0.21 | 0.06 | 0.18 | 0.29 |
| Heather | 0.35 | 0.20 | 0.05 | 0.08 | 0.32 |

568

569 3.2 Potential and actual evapotranspiration

570 The modeled ET_a is in agreement with the measured ET_a , with some exceptions at the onset of
 571 dry out events (Fig. 9). In general, reduction of ET_p to ET_a is modeled a few days later than
 572 emerges from measurements. The cumulative $ET_{a,mod}$ over the measurement period (May-
 573 October 2013) deviates 21 mm (13 %), -13 mm (-7 %), 5 mm (2 %) and -3 mm (-2 %) from
 574 the measured ET_a of the sand, moss, grass and heather lysimeters respectively. The results of
 575 modeled vs. measured ET_a for non-water stressed ($ET_a = ET_p$) and water stresses conditions
 576 ($ET_{a,mod} < ET_p$) are summarized in Table 7.

577 We did not calibrate our model, e.g. by adjusting soil hydraulic properties, because
 578 several processes outlined by Allen et al. (1991) and wall flow (Cameron et al., 1992;Corwin,
 579 2000;Till and McCabe, 1976;Saffigna et al., 1977) affect lysimeter measurements of ET_a and
 580 drainage. We suspect that wall flow caused the slightly earlier reduction of ET_p to ET_a at the
 581 onset of dry out events than was simulated by the model. Wall flow leads to a quicker
 582 exfiltration of rainwater and a subsequent lower moisture content in the lysimeter, and
 583 therefore a slightly earlier timing of drought compared to the model. Since wall flow does not
 584 occur in the undisturbed vegetation outside the lysimeters, calibrating e.g. soil hydraulic
 585 properties using measured surface and drainage fluxes in the objective function could lead to
 586 biased characterizations of the soil hydraulic properties and erroneous simulations of soil
 587 water flow and ET_a .

588 In our simulations, we neglected vapor flow within the soil and moss layer. Due to
 589 temperature and potential gradients, vapor fluxes may occur through the soil and moss layer
 590 in upward and downward direction by diffusion. Vapor flow may occur by advection as well,
 591 e.g. through macro pores. Water and vapor flows act together and are hard to distinguish
 592 between. Modelling and lab experiments show a minor cumulative effect of vapor flow on
 593 evaporation for moist and temperate climates. Soil evaporation in a temperate climate for
 594 loamy sand in Denmark was only slightly smaller (1.5 %) than a simulation excluding vapor

595 flow (Schelde et al., 1998). Experiments of Price et al. (2009) show that only 1% of the total
596 water flux was caused by vapor flow in columns of *Sphagnum* moss. Nevertheless, for a dry
597 and warm Mediterranean climate – different from ours – Boulet et al. (1997) found a
598 dominant vapor flux down to a depth of 25 cm in a bare soil during 11 days in a dry and warm
599 Mediterranean climate. Because large temperature and potential gradients occur when $ET_a \neq$
600 ET_p , vapor flow could especially become dominant in the water limited phase of evaporation.
601 We compared the model performance between dry ($ET_{a,mod} \neq ET_p$) and wet ($ET_{a,mod} = ET_p$)
602 days in Fig. 10. The model performance in both moisture conditions is comparable (*RMSE*
603 sand: dry = 0.40, wet = 0.46, *RMSE* moss: dry = 0.30, wet = 0.39), suggesting that our
604 simplified model could describe the dominant processes and the simulation of vapor flow was
605 not required for the temperate climate of our study area.

606 One would expect oasis effects to occur in the vicinity of the lysimeters, because
607 freely draining lysimeters must saturate at the bottom of the lysimeter tank before water
608 drains out. This enlarges the water availability inside the lysimeters compared to its
609 groundwater independent surroundings and occasionally leads to a situation in which the
610 vegetation inside the lysimeters is still transpiring, while the vegetation outside the lysimeters
611 becomes water stressed and heats up. In such situation advection of sensible heat generated in
612 the vicinity of the lysimeters could contribute to the available energy for lysimeter
613 evapotranspiration. However, calculated ET_p was seldom smaller than measured lysimeter
614 ET_a , indicating that oasis effects were absent. Furthermore, if oasis effects were prominent,
615 systematic underestimation of modeled lysimeter ET_a would occur, since we ignored the
616 possible contribution of heat advection. Note that it is very unlikely that oasis effects affected
617 the back-calculated surface resistances (Table 5), since these were based on days after rain
618 events for which we may assume ET_a to be equal to ET_p for both the lysimeters and their
619 surroundings.

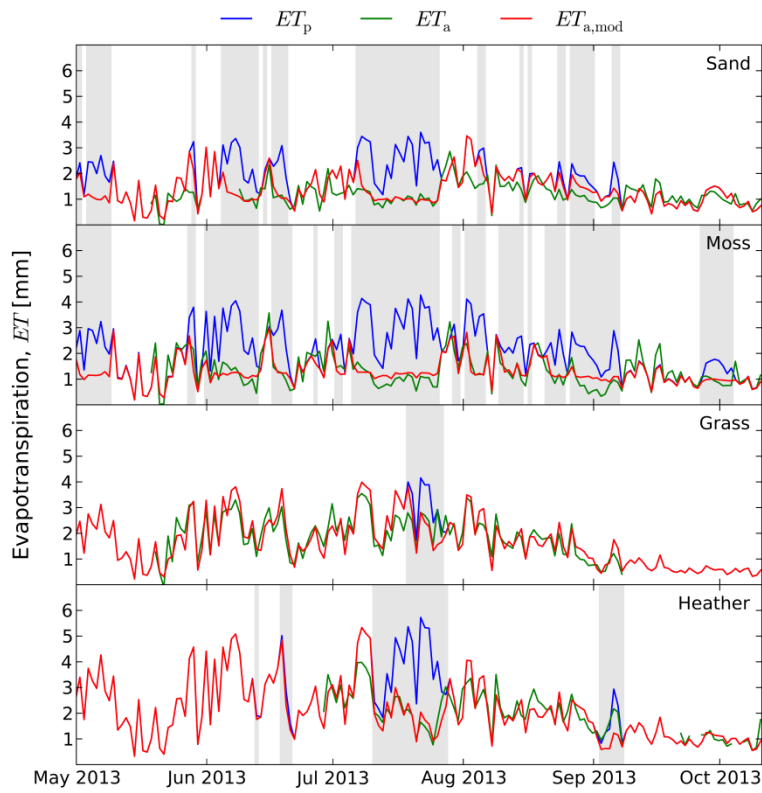
620 Neglecting feedbacks of drought on the transpiring leaf area and thereby the surface
621 resistance (i.e. using a fixed r_s) of heather and dry grassland vegetation leads to an
622 overestimation of cumulative ET_a of 7 to 9 % for years with relatively severe drought (Table
623 7). The delayed drought response of these vegetation types is therefore of importance to water
624 balance studies, especially when, according to the expectations, summers become dryer as a
625 result of a changing climate. Longer recordings of ET_a in heathland and grassland are required
626 to understand and parameterize the drought response of these vegetation types in coupled
627 plant physiological and hydro-meteorological models.

628 To our knowledge, this paper describes for the first time the evaporation
629 characteristics of a moss surface in a dune ecosystem in a temperate climate. The evaporation
630 rate of the dense moss mat *Campylopus introflexus* is 5 % larger than the evaporation rate of
631 bare sand. *Campylopus introflexus* forms dense moss mats and of the moss species
632 investigated by Voortman et al. (2013), it has the largest water holding capacity. Voortman et
633 al. (2013) hypothesized that moss covered soils could be more economical with water than
634 bare soils, since the unsaturated hydraulic properties of moss layers ~~temper~~reduce the
635 magnitude of evaporation under relatively moist conditions. Our simulations of evaporation
636 from the more open structured *Hypnum cupressiforme* moss species (common in coastal
637 dunes), which primarily differs in moisture content near saturation compared to *Campylopus*
638 *introflexus* (0.20 instead of 0.61), confirms this hypothesis. The simulated evaporation rate for
639 this species was 29 % lower than the evaporation rate of bare soil. From both our
640 measurements and model simulations, xerophytic (drought tolerant) mosses appear to be very
641 economical with water: their evaporation rate is comparable with that of bare sand, or lower.

642 *Campylopus introflexus* is considered an invasive species in the Northern Hemisphere
643 and was first discovered in Europe in 1941 (Klinck, 2010). Considering the large difference in
644 yearly evaporation between *Hypnum cupressiforme* and *Campylopus introflexus* species (90
645 mm), the invasion of the *Campylopus introflexus* could have had negative impacts on water
646 resources in specific areas which were previously dominated by more open structured moss
647 species with poorer water retention characteristics. For sustainable management of
648 groundwater resources in coastal and inland sand dunes, an accurate estimate of the
649 groundwater recharge is required. For consultancy about the availability of water, moss
650 species cannot be categorized in a singular plant functional type, since the modulating effect
651 of the moss cover is species specific. However, in terms of water retention characteristics, the
652 species investigated by Voortman et al. (2013) are distinguished from each other by the water
653 holding capacity near saturation (θ_0 , Appendix A), which is easily measured ~~by~~-in a
654 laboratory. Moss species could be categorized by this characteristic.

655 Mosses and lichens are common in early successional stages after colonizing and
656 stabilizing drift sand or as understory vegetation in heathlands or grasslands. Vascular plants
657 might benefit from the presence of certain moss species as more water may be conserved in
658 the root zone. On the other hand, field observations show that moss- and lichen-rich
659 vegetation can persist for many decades (Daniëls et al., 2008). Detailed measurements of
660 understory evaporation in heathlands and grasslands are required to unravel the ecological
661 interactions between mosses and vascular plants.

662

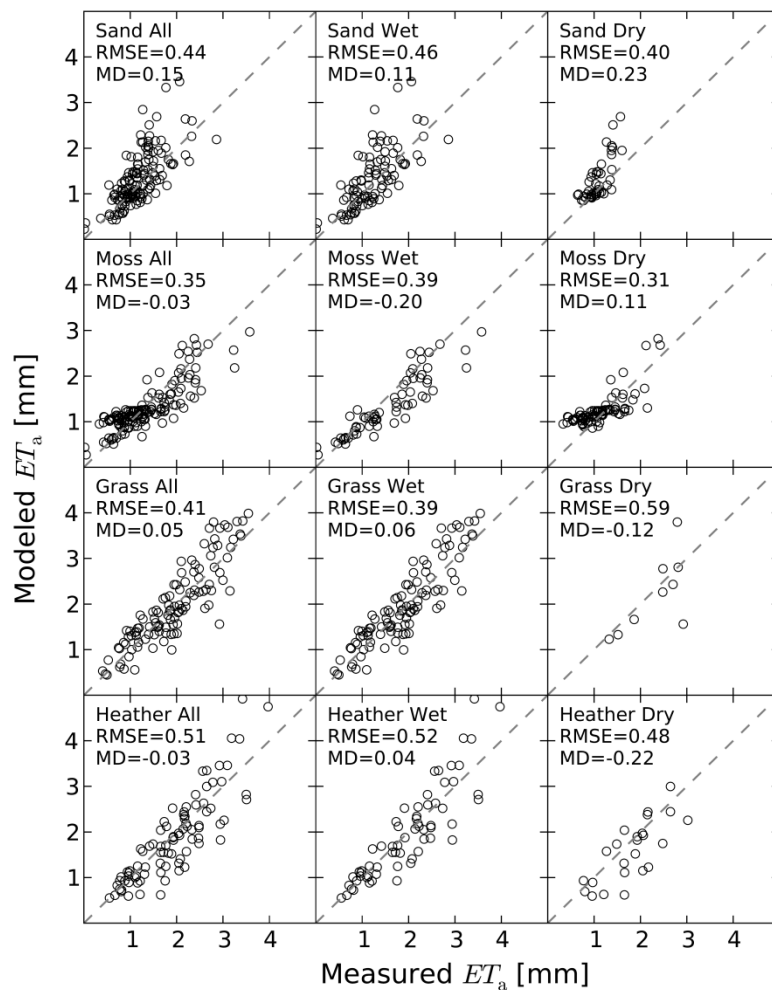


663

664 Fig. 9. Measured and modeled daily ET for the four lysimeters. Grey bars indicate time
665 periods where $ET_{a,mod}$ is smaller than ET_p , i.e. when evapotranspiration was water limited.

666

667



668

669 Fig. 10. Measured vs. modeled ET_a of the lysimeters for all, wet ($ET_{a,mod} = ET_p$) and
 670 ($ET_{a,mod} \neq ET_p$) days. Dotted lines represent the 1:1 lines.

671

672 Table 7. Modeled ET_p and ET_a for different surfaces in a lysimeter (lys.) and for a situation
 673 with deep groundwater levels (gw. ind.) for the year 2013.

| | ET_p (mm) | ET_a lys. (mm) | ET_a gw. ind. (mm) |
|---------------------------------|-------------|------------------|----------------------|
| Bare sand | 400 | 295 | 258 |
| Moss (<i>Campylopus int.</i>) | 468 | 312 | 272 |
| Moss (<i>Hypnum cup.</i>) | 468 | --- | 182 |
| Grass | 392 | 350 | 333 |
| Grass no dieback | 429 (+9%) | 382 (+9%) | 362 (+9%) |
| Heather | 549 | 460 | 391 |
| Heather no dieback | 610 (+11%) | 499 (+8%) | 420 (+7%) |

674

675

676

677 **4 Conclusions**

678 In this study the net longwave radiation (R_{nl}) appeared to be one of the largest energy fluxes
679 in dune vegetation. The poor performance of the calibrated FAO-56 approach for simulating
680 R_{nl} for hourly time steps illustrates that this energy flux has attracted insufficient attention in
681 evapotranspiration research. The novel approach presented in this study to simulate R_{nl}
682 outperformed the calibrated FAO-56 approach and forms an accurate alternative for
683 estimating R_{nl} .

684 A relatively simple hydrological model could be used to simulate evapotranspiration
685 of dry dune vegetation with satisfactory results. Improvements in terms of climate robustness
686 would be especially achieved if plant physiological processes were integrated in the hydro-
687 meteorological model. Without considering the effects of dry spells on the surface resistance
688 (r_s) of grassland and heathland vegetation, ET_a would be overestimated with 9 % and 7 % for
689 years with relatively severe drought (drought events with a reoccurrence of once per five
690 years).

691 Moss species are very economical with water. The evaporation of moss surfaces is
692 comparable or even lower than bare sand. By promoting moss dominated ecosystems in
693 coastal and inland dunes, the evapotranspiration could be reduced considerably, to the benefit
694 of the groundwater system. Differences in evaporation between moss species are large and
695 should be considered in water balance studies.

696 Long-term measurements of ET_a in heathland and grassland are required to study
697 | feedbacks between climate and plant physiological processes ~~which allows in order to~~
698 | ~~integrate the integration of~~ the drought response of natural vegetation in coupled plant
699 | physiological and hydro-meteorological models. To understand the ecological interaction
700 | between mosses and vascular plants, detailed measurements of understory evaporation in
701 | heathlands and grasslands are required.

702

703 **Acknowledgements**

704 This study was carried out within the joint research programme of the Dutch Water Utility
705 sector (<http://www.kwrwater.nl/BTO>), and the project Climate Adaptation
706 for Rural Areas (CARE), which was funded by the Knowledge for Climate Program
707 (<http://knowledgeforclimate.climateresearchnetherlands.nl/climateadaptationforruralareas>).
708 We thank the staff of Vitens for their permission to perform hydro-meteorological
709 measurements in one of their drinking water extraction sites.

710

711 **Appendix A. Soil hydraulic properties for the simulation of unsaturated flow with**
712 **Hydrus-1D**

713

714 Unsaturated flow in Hydrus 1D is described by a modified form of Richards' equation:

$$715 \quad \frac{\partial \theta}{\partial t} = \frac{\partial}{\partial z} \left(K \frac{\partial h}{\partial z} + K \right), \quad 13$$

716

717 Where K is the unsaturated conductivity [LT^{-1}], z is the vertical coordinate [L] and t is the
718 time [T]. The soil hydraulic properties were assumed to be described by the Mualum van
719 Genuchten functions:

720

$$721 \quad \theta(h) = \theta_r + \frac{\theta_0 - \theta_r}{\left[1 + |\alpha h|^n\right]^m}, \quad 14$$

722

$$723 \quad K(\theta) = K_0 S_e^l [1 - (1 - S_e^{1/m})^m]^2, \quad 15$$

724 with

$$725 \quad S_e(h) = \frac{\theta(h) - \theta_r}{\theta_0 - \theta_r}, \quad 16$$

726

727 where θ is the volumetric water content [L^3/L^3], h is the soil water pressure head [L], θ_0 is an
728 empirical parameter matching measured and modeled θ [L^3/L^3], θ_r is the residual water
729 content [L^3/L^3] and α [L^{-1}] and n [-] are empirical shape parameters of the retention function,
730 K_0 is an empirical parameter, matching measured and modeled K [LT^{-1}], S_e is the effective
731 saturation [-], l is the pore-connectivity parameter [-] and m ($=1-1/n$) [-] is an empirical
732 parameter. Drying retention data of two soil samples collected next to each lysimeter at 5 and
733 15 cm depth were used to fit a retention function with the RETC code (Van Genuchten et al.,
734 1991). Hysteresis in the retention function was accounted for by assuming the retention curve
735 parameter α for the wetting curve (α_{wet}) to be twice as large as α of the drying retention curve
736 (α_{dry}) (Šimůnek et al., 1999). The unsaturated hydraulic conductivity parameters l and K_0 were
737 estimated using the Rosetta database and pedotransfer functions, providing the fitted drying
738 retention curve parameters as input (Schaap et al., 2001). Average parameter values per
739 lysimeter are summarized in Table A1.

740 The hydraulic properties of the 15 cm long wick, guiding drainage water below the
741 lysimeter into the tipping bucket, were taken from Knutson and Selker (1994) who analyzed

742 the same brand and type of wick, i.e. Peperell ½ inch. The K_0 of the wick was adjusted to
 743 correct for the smaller cross sectional area of the wick compared to the cross sectional area of
 744 the lysimeter in the 1D model simulation. (Table A1).

745

746 Table A1. Hydraulic parameter values of lysimeter soils.

| | θ_r | θ_0 | α_{dry} | α_{wet} | n | K_0 | L |
|-----------|------------|------------|---------------------|---------------------|-------|--------|--------|
| | [-] | [-] | [cm ⁻¹] | [cm ⁻¹] | [-] | [cm/h] | [-] |
| Bare Sand | 0.01 | 0.367 | 0.023 | 0.046 | 2.945 | 1.042 | -0.401 |
| Moss | 0.01 | 0.397 | 0.019 | --- | 2.335 | 0.734 | -0.173 |
| Grass | 0.01 | 0.401 | 0.025 | 0.050 | 2.071 | 1.119 | -0.278 |
| Heather | 0.01 | 0.392 | 0.018 | 0.036 | 2.581 | 0.679 | -0.186 |
| Wick | 0.00 | 0.630 | 0.098 | 0.196 | 3.610 | 2.180 | 0.500 |

747

748 The heterogeneous pore structure of the moss material was described by the functions
 749 of Durner (1994):

750

$$751 \quad S_e = w_1 \left(1 + [\alpha_1 h]^{n_1}\right)^{-m_1} + w_2 \left(1 + [\alpha_2 h]^{n_2}\right)^{-m_2}, \quad 17$$

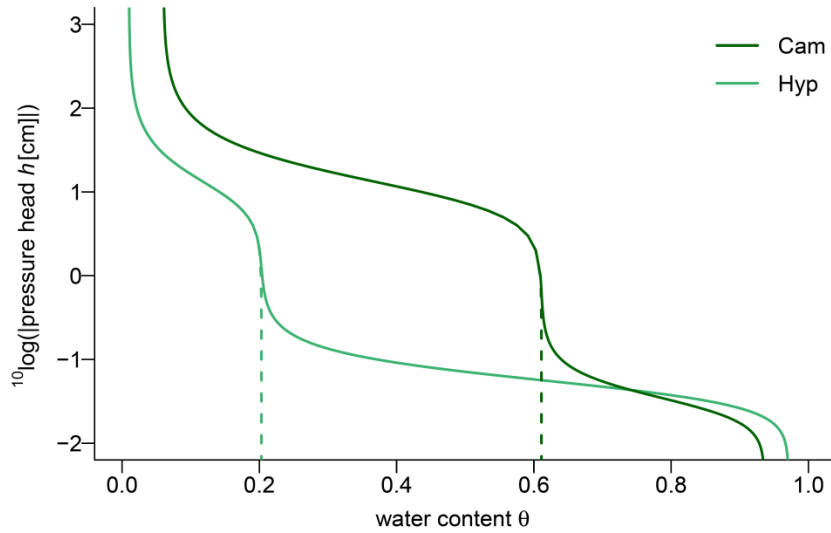
752

$$753 \quad K(S_e) = K_s \frac{\left(w_1 S_{e_1} + w_2 S_{e_2}\right)^l \left(w_1 \alpha_1 \left[1 - \left(1 - S_{e_1}^{1/m_1}\right)^{m_1}\right] + w_2 \alpha_2 \left[1 - \left(1 - S_{e_2}^{1/m_2}\right)^{m_2}\right]\right)^2}{\left(w_1 \alpha_1 + w_2 \alpha_2\right)^2}, \quad 18$$

754

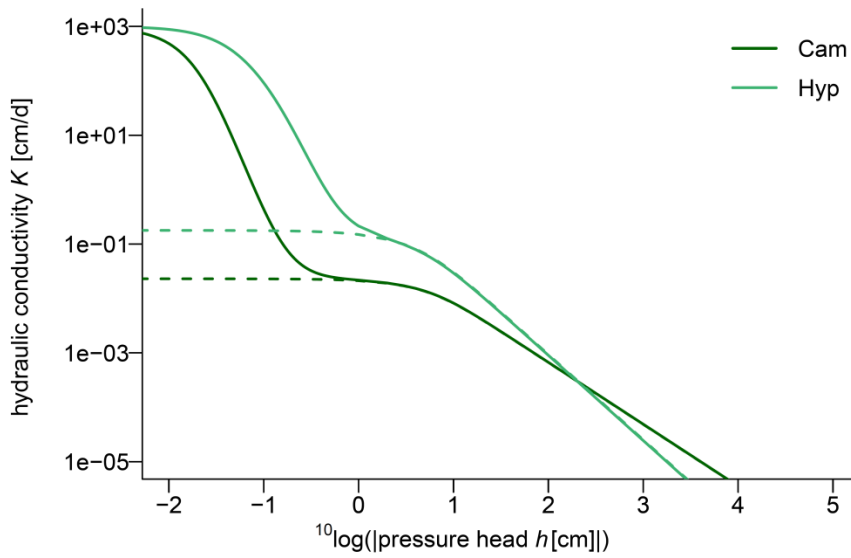
755 Where w_1 and w_2 are weighting factors for two distinct pore systems of the moss layer; a
 756 capillary pore system (subscript 1) and a macro pore system active near saturation ($h > -1$ cm,
 757 subscript 2) and K_s is the hydraulic conductivity at saturation. Average hydraulic parameters
 758 of the capillary pore system and the volumetric portion of the macro pore system of the moss
 759 species *Campylopus introflexus* and *Hypnum cupressiforme* were taken from Voortman et al.
 760 (2013) (illustrated with dotted lines in Fig. A1 and Fig. A2). The α_2 parameter was fitted to
 761 the functions of Voortman et al. (2013) using $K_s = 1000$ cm/d and $n_2 = 2$ by minimizing the
 762 *RMSE* by generalized reduced gradient nonlinear optimization. Hydraulic parameter values
 763 are listed in Table A2.

764



765
766
767
768
769

Fig. A1. Water retention functions of two moss species: *Campylopus introflexus* and *Hypnum cupressiforme*. The dotted lines indicate the contribution of the capillary pore system characterized by Voortman et al. (2013).



770
771
772
773
774

Fig. A2. Hydraulic conductivity functions for two moss species: *Campylopus introflexus* and *Hypnum cupressiforme*. The dotted lines indicate the contribution of the capillary pore system characterized by Voortman et al. (2013).

775 Table A2. Hydraulic parameter values of the two moss species.

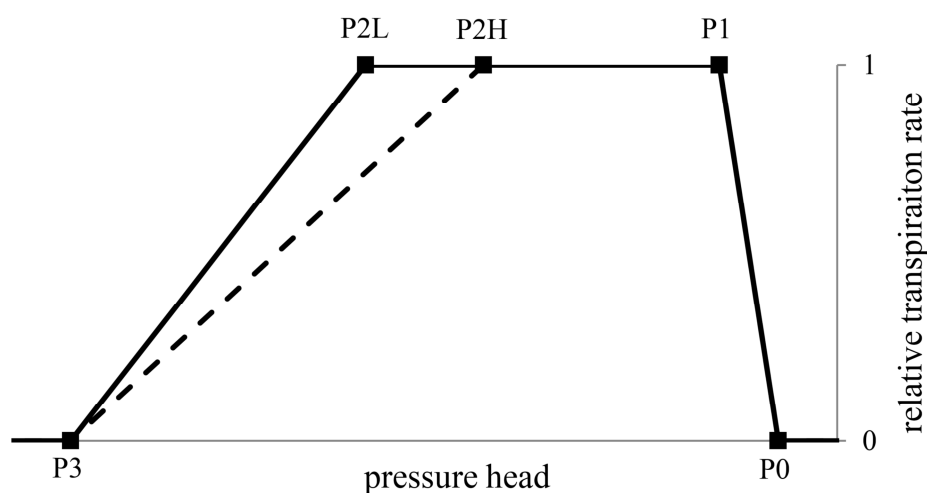
| | θ_r | θ_s | α_1 | n | K_s | l | w_2 | α_2 | n_2 |
|------------------------|------------|------------|---------------------|------|--------|-------|-------|---------------------|-------|
| | [-] | [-] | [cm ⁻¹] | [-] | [cm/h] | [-] | [-] | [cm ⁻¹] | [-] |
| <i>Campylopus int.</i> | 0.060 | 0.936 | 0.080 | 2.25 | 41.67 | -2.69 | 0.371 | 45.89 | 2.00 |
| <i>Hypnum cup.</i> | 0.010 | 0.971 | 0.013 | 2.17 | 41.67 | -2.37 | 0.800 | 16.61 | 2.00 |

776

777 **Appendix B. Feddes function used in the Hydrus 1D model to simulate the closure of leaf**
 778 **stomata during water stressed periods.**

779
 780 The Feddes function (Feddes et al., 1978) describes the relative transpiration rate in relation to
 781 the soil water pressure head (Fig. B1) (being 0 if transpiration ceases and 1 if it equals
 782 potential rate). Near positive pressure heads, root water uptake ceases due to oxygen stress
 783 (P0). At the dry end of the function, root water uptake ceases (P3). The moment at which
 784 transpiration becomes limited due to moisture stress is dependent on the potential
 785 transpiration rate. At a high potential transpiration rate (5 mm/d in the model simulation) leaf
 786 stomata start to close earlier (P2H) than under low potential transpiration rate (P2L, 1 mm/d
 787 in the model simulation). Values for the parameters of Fig. B1 are listed in Table B1.

788
 789



790
 791 Fig. B1. The relative transpiration rate as function of soil water pressure head according to
 792 Feddes et al. (1978).

793
 794 Table B1. Parameters of the water stress reduction function used in the Hydrus 1D model.

| P0 | P1 | P2H | P2L | P3 | r2H | r2L |
|------|------|------|-------|-------|--------|--------|
| [cm] | [cm] | [cm] | [cm] | [cm] | [mm/h] | [mm/h] |
| -10 | -25 | -300 | -1000 | -8000 | 5 | 1 |

795
 796
 797

798 **References**

799 Allen, R. G., Pruitt, W. O., and Jensen, M. E.: Environmental requirements of lysimeters, in: Lysimeters for
800 evapotranspiration and environmental measurements, edited by: Allen, R. G., Howell, T. A., Pruitt, W. O., Walter, I.
801 A., and Jensen, M. E., American Society of Civil Engineers, New York, 170-181, 1991.
802 Allen, R. G., Pereira, L. S., Raes, D., and Smith, M.: Crop Evapotranspiration-Guidelines for Computing Crop Water
803 Requirements, FAO Irrigation and drainage paper 56. United Nations Food and Agriculture Organization, Rome,
804 1998.
805 ASCE-EWRI: The ASCE Standardized Reference Evapotranspiration Equation, Environmental and Water Resources
806 Institute of the American Society of Civil Engineers, Reston, Virginia, USA, 2005.
807 Bastiaanssen, W. G. M., Menenti, M., Feddes, R. A., and Holtslag, A. A. M.: A remote sensing surface energy balance
808 algorithm for land (SEBAL). 1. Formulation, Journal of Hydrology, 212-213, 198-212,
809 [http://dx.doi.org/10.1016/S0022-1694\(98\)00253-4](http://dx.doi.org/10.1016/S0022-1694(98)00253-4), 1998.
810 Blonquist Jr, J. M., Allen, R. G., and Bugbee, B.: An evaluation of the net radiation sub-model in the ASCE
811 standardized reference evapotranspiration equation: Implications for evapotranspiration prediction, Agricultural
812 Water Management, 97, 1026-1038, <http://dx.doi.org/10.1016/j.agwat.2010.02.008>, 2010.
813 Boulet, G., Braud, I., and Vauclin, M.: Study of the mechanisms of evaporation under arid conditions using a detailed
814 model of the soil-atmosphere continuum. Application to the EFEDA I experiment, Journal of Hydrology, 193, 114-
815 141, [http://dx.doi.org/10.1016/S0022-1694\(96\)03148-4](http://dx.doi.org/10.1016/S0022-1694(96)03148-4), 1997.
816 Brunt, D.: Notes on radiation in the atmosphere. I, Q. J. R. Meteorol. Soc., 58, 389-420, 10.1002/qj.49705824704,
817 1932.
818 Cameron, K. C., Smith, N. P., McLay, C. D. A., Fraser, P. M., McPherson, R. J., Harrison, D. F., and Harbottle, P.:
819 Lysimeters Without Edge Flow: An Improved Design and Sampling Procedure, Soil Sci. Soc. Am. J., 56, 1625-1628,
820 10.2136/sssaj1992.03615995005600050048x, 1992.
821 Campbell Scientific Inc.: Model HFP01 SC Self-Calibrating Soil Heat Flux Plate, 24, 2014.
822 Corwin, D. L.: Evaluation of a simple lysimeter-design modification to minimize sidewall flow, Journal of
823 Contaminant Hydrology, 42, 35-49, [http://dx.doi.org/10.1016/S0169-7722\(99\)00088-1](http://dx.doi.org/10.1016/S0169-7722(99)00088-1), 2000.
824 Daniëls, F. J. A., Minarski, A., and Lepping, O.: Dominance pattern changes of a lichen-rich corynephorus grassland
825 in the inland of The Netherlands, Annali di Botanica n.s., VIII, 9-19, 2008.
826 Delpla, I., Jung, A. V., Baures, E., Clement, M., and Thomas, O.: Impacts of climate change on surface water quality
827 in relation to drinking water production, Environment International, 35, 1225-1233,
828 <http://dx.doi.org/10.1016/j.envint.2009.07.001>, 2009.
829 Dolman, A. J.: Predicting evaporation from an oak forest, Ph.D, University of Groningen, 91 pp., 1987.
830 Durner, W.: Hydraulic conductivity estimation for soils with heterogeneous pore structure, Water Resour. Res., 30,
831 211-223, 10.1029/93wr02676, 1994.
832 Feddes, R. A., Kowalik, P. J., and Zaradny, H.: Simulation of Field Water Use and Crop Yield, Pudoc Wageningen,
833 1978.
834 Federer, C. A., Vörösmarty, C., and Fekete, B.: Intercomparison of Methods for Calculating Potential Evaporation in
835 Regional and Global Water Balance Models, Water Resour. Res., 32, 2315-2321, 10.1029/96wr00801, 1996.
836 Friedl, M. A.: Relationships among Remotely Sensed Data, Surface Energy Balance, and Area-Averaged Fluxes over
837 Partially Vegetated Land Surfaces, Journal of Applied Meteorology, 35, 2091-2103, 10.1175/1520-
838 0450(1996)035<2091:rarsds>2.0.co;2, 1996.
839 Fuchs, M., and Tanner, C. B.: Surface Temperature Measurements of Bare Soils, Journal of Applied Meteorology, 7,
840 303-305, 10.1175/1520-0450(1968)007<0303:stmobs>2.0.co;2, 1968.
841 Gavilán, P., Estévez, J., and Berengena, J.: Comparison of standardized reference evapotranspiration equations in
842 Southern Spain, Journal of Irrigation and Drainage Engineering, 134, 1-12, 2008.
843 Gavriliev, R. I.: Thermal properties of soils and surface covers, in: Thermal Analysis, Construction, and Monitoring
844 Methods for Frozen Ground, edited by: Esch, D. C., American Society of Civil Engineers, Reston, Virginia, USA, 277-
845 295, 2004.
846 Gubler, S., Gruber, S., and Purves, R. S.: Uncertainties of parameterized surface downward clear-sky shortwave and
847 all-sky longwave radiation, Atmos. Chem. Phys., 12, 5077-5098, 10.5194/acp-12-5077-2012, 2012.
848 Hollinger, D. Y., Ollinger, S. V., Richardson, A. D., Meyers, T. P., Dail, D. B., Martin, M. E., Scott, N. A.,
849 Arkebauer, T. J., Baldocchi, D. D., Clark, K. L., Curtis, P. S., Davis, K. J., Desai, A. R., Dragonik, D., Goulden, M. L.,
850 Gu, L., Katul, G. G., Pallardy, S. G., Pawu, K. T., Schmid, H. P., Stoy, P. C., Suyker, A. E., and Verma, S. B.: Albedo
851 estimates for land surface models and support for a new paradigm based on foliage nitrogen concentration, Global
852 Change Biology, 16, 696-710, 2010.
853 Irmak, S., Howell, T. A., Allen, R. G., Payero, J. O., and Martin, D. L.: Standardized ASCE Penman-Monteith: Impact of
854 sum-of-hourly vs. 24-hour timestep computations at reference weather station sites, Transactions of the American
855 Society of Agricultural Engineers, 48, 1063-1077, 2005.
856 Irmak, S., Mutibwa, D., and Payero, J. O.: Net radiation dynamics: Performance of 20 daily net radiation models as
857 related to model structure and intricacy in two climates, Transactions of the ASABE, 53, 1059-1076, 2010.
858 Jones, H. G.: Application of Thermal Imaging and Infrared Sensing in Plant Physiology and Ecophysiology, in:
859 Advances in Botanical Research, Academic Press, 107-163, 2004.
860 Kay, A. L., Bell, V. A., Blyth, E. M., Crooks, S. M., Davies, H. N., and Reynard, N. S.: A hydrological perspective on
861 evaporation: historical trends and future projections in Britain, Journal of Water and Climate Change, 4, 193-208,
862 doi:10.2166/wcc.2013.014, 2013.
863 Klinck, J.: NOBANIS Invasive Alien Species Fact Sheet *Campylopus introflexus*, From: Online Database of the North
864 European and Baltic Network on Invasive Alien Species - NOBANIS, 2010.
865 Knutson, J. H., and Selker, J. S.: Unsaturated hydraulic conductivities of fiberglass wicks and designing capillary wick
866 pore-water samplers, Soil Science Society of America Journal, 58, 721-729, 1994.
867 Kustas, W. P., and Daughtry, C. S. T.: Estimation of the soil heat flux/net radiation ratio from spectral data,
868 Agricultural and Forest Meteorology, 49, 205-223, [http://dx.doi.org/10.1016/0168-1923\(90\)90033-3](http://dx.doi.org/10.1016/0168-1923(90)90033-3), 1990.

869 Kustas, W. P., Zhan, X., and Schmugge, T. J.: Combining Optical and Microwave Remote Sensing for Mapping Energy
870 Fluxes in a Semiarid Watershed, *Remote Sensing of Environment*, 64, 116-131, [http://dx.doi.org/10.1016/S0034-4257\(97\)00176-4](http://dx.doi.org/10.1016/S0034-4257(97)00176-4), 1998.

871 Ladekarl, U. L., Rasmussen, K. R., Christensen, S., Jensen, K. H., and Hansen, B.: Groundwater recharge and
872 evapotranspiration for two natural ecosystems covered with oak and heather, *Journal of Hydrology*, 300, 76-99,
873 <http://dx.doi.org/10.1016/j.jhydrol.2004.05.003>, 2005.

874 Liakatas, A., Clark, J. A., and Monteith, J. L.: Measurements of the heat balance under plastic mulches. Part I.
875 Radiation balance and soil heat flux, *Agricultural and Forest Meteorology*, 36, 227-239,
876 [http://dx.doi.org/10.1016/0168-1923\(86\)90037-7](http://dx.doi.org/10.1016/0168-1923(86)90037-7), 1986.

877 Linacre, E. T.: Net Radiation to Various Surfaces, *Journal of Applied Ecology*, 6, 61-75, 10.2307/2401301, 1969.

878 Liu, S., Graham, W. D., and Jacobs, J. M.: Daily potential evapotranspiration and diurnal climate forcings: influence
879 on the numerical modelling of soil water dynamics and evapotranspiration, *Journal of Hydrology*, 309, 39-52, 2005.

880 López-Urrea, R., Olalla, F. M. d. S., Fabeiro, C., and Moratalla, A.: An evaluation of two hourly reference
881 evapotranspiration equations for semiarid conditions, *Agricultural Water Management*, 86, 277-282, 2006.

882 Makkink, G. G.: Testing the Penman formula by means of lysimeters, *J. Inst. Wat. Engrs.*, 11, 277-288, 1957.

883 Matsui, H.: Comparison of Net Longwave Radiation Equation in Penman-Type Evapotranspiration Equation,
884 *Transactions of The Japanese Society of Irrigation, Drainage and Rural Engineering*, 78, 531-536,
885 <http://dx.doi.org/10.11408/jsidre.78.531>, 2010.

886 Miranda, A. C., Jarvis, P. G., and Grace, J.: Transpiration and evaporation from heather Moorland, *Boundary-Layer
887 Meteorology*, 28, 227-243, 10.1007/bf00121306, 1984.

888 Monteith, J. L., and Unsworth, M. H.: *Principles of Environmental Physics*, Edward Arnold, London, 1990.

889 Moors, E. J.: *Water Use of Forest in the Netherlands*, Ph.D, Vrije Universiteit Amsterdam, 2012.

890 Nozue, K., and Maloof, J. N.: Diurnal regulation of plant growth*, *Plant, Cell & Environment*, 29, 396-408,
891 10.1111/j.1365-3040.2005.01489.x, 2006.

892 Oke, T. R.: *Boundary Layer Climates*, Methuen & Co Ltd, London, 372 pp., 1978.

893 Penman, H. L.: Natural evaporation from open water, bare soil and grass, *Proceedings of the Royal Society of London
894 Series a-Mathematical and Physical Sciences*, 193, 120-145, 10.1098/rspa.1948.0037, 1948.

895 Perera, K. C., Western, A. W., Nawarathna, B., and George, B.: Comparison of hourly and daily reference crop
896 evapotranspiration equations across seasons and climate zones in Australia, *Agricultural Water Management*, 148,
897 84-96, <http://dx.doi.org/10.1016/j.agwat.2014.09.016>, 2015.

898 Price, J. S., Edwards, T. W. D., Yi, Y., and Whittington, P. N.: Physical and isotopic characterization of evaporation
899 from Sphagnum moss, *Journal of Hydrology*, 369, 175-182, 2009.

900 Proctor, M. C. F., Oliver, M. J., Wood, A. J., Alpert, P., Stark, L. R., Cleavitt, N. L., and Mishler, B. D.: Desiccation-
901 tolerance in bryophytes: A review, *The Bryologist*, 110, 595-621, 10.1639/0007-
902 2745(2007)110[595:DIBAR]2.0.CO;2, 2007.

903 Qiu, G. Y., Yano, T., and Momii, K.: An improved methodology to measure evaporation from bare soil based on
904 comparison of surface temperature with a dry soil surface, *Journal of Hydrology*, 210, 93-105, 1998.

905 Saffigna, P. G., Kenney, D. R., and Tanner, C. B.: Lysimeter and field measurements of chloride and bromide leaching
906 in an uncultivated loamy sand, *Soil Sci. Soc. Am. J.*, 41, 478-482, 1977.

907 Saito, H., and Šimůnek, J.: Effects of meteorological models on the solution of the surface energy balance and soil
908 temperature variations in bare soils, *Journal of Hydrology*, 373, 545-561,
909 <http://dx.doi.org/10.1016/j.jhydrol.2009.05.019>, 2009.

910 Schaap, M. G., Leij, F. J., and Van Genuchten, M. T.: Rosetta: A computer program for estimating soil hydraulic
911 parameters with hierarchical pedotransfer functions, *Journal of Hydrology*, 251, 163-176, 10.1016/S0022-
912 1694(01)00466-8, 2001.

913 Schelde, K., Thomsen, A., Heidmann, T., Schjønning, P., and Jansson, P. E.: Diurnal fluctuations of water and heat
914 flows in a bare soil, *Water Resources Research*, 34, 2919-2929, 10.1029/98wr02225, 1998.

915 Shuttleworth, W. J.: Putting the 'vap' into evaporation, *Hydrology and Earth System Sciences*, 11, 210-244, 2007.

916 Šimůnek, J., Kodešová, R., Gribb, M. M., and van Genuchten, M. T.: Estimating hysteresis in the soil water retention
917 function from cone permeameter experiments, *Water Resources Research*, 35, 1329-1345, 10.1029/1998wr900110,
918 1999.

919 Šimůnek, J., Šejna, M., Saito, H., Sakai, M., and van Genuchten, M. T.: The Hydrus-1D Software Package for
920 Simulating the movement of water, heat, and multiple solutes in variably saturated media, version 4.0, HYDRUS
921 Software Series 3, Department of Environmental Sciences, University of California Riverside, Riverside, 2008.

922 Su, Z.: The Surface Energy Balance System (SEBS) for estimation of turbulent heat fluxes, *Hydrology and Earth
923 System Sciences*, 6, 85-99, 2002.

924 Temesgen, B., Eching, S., and Frame, K.: Comparing net radiation estimation methods: CIMIS versus Penman-
925 Monteith, *Journal of Irrigation and Drainage Engineering*, 133, 265-271, 10.1061/(ASCE)0733-
926 9437(2007)133:3(265), 2007.

927 Till, A. R., and McCabe, T. P.: Sulfur leaching and lysimeter characterization, *Soil Sci.*, 121, 44-47, 1976.

928 Van Bavel, C. H. M., and Hillel, D. I.: Calculating potential and actual evaporation from a bare soil surface by
929 simulation of concurrent flow of water and heat, *Agricultural Meteorology*, 17, 453-476,
930 [http://dx.doi.org/10.1016/0002-1571\(76\)90022-4](http://dx.doi.org/10.1016/0002-1571(76)90022-4), 1976.

931 Van de Griend, A. A., and Owe, M.: Bare soil surface resistance to evaporation by vapor diffusion under semiarid
932 conditions, *Water Resources Research*, 30, 181-188, 10.1029/93wr02747, 1994.

933 Van Genuchten, M. T.: A closed-form equation for predicting the hydraulic conductivity of unsaturated soils, *Soil
934 Science Society of America Journal*, 44, 892-898, 10.2136/sssaj1980.03615995004400050002x, 1980.

935 Van Genuchten, M. T., Leij, F. J., and Yates, S. R.: *The RETC Code for Quantifying the Hydraulic Functions of
936 Unsaturated Soils*, Version 1.0, Salinity Laboratory, USDA, ARS, Riverside, California, 1991.

937 van Vliet, M. T. H., and Zwolsman, J. J. G.: Impact of summer droughts on the water quality of the Meuse river,
938 *Journal of Hydrology*, 353, 1-17, <http://dx.doi.org/10.1016/j.jhydrol.2008.01.001>, 2008.

939 Van Wijk, W. R., and Scholte Ubung, D. W.: Radiation, in: *Physics of plant environment*, edited by: Van Wijk, W. R.,
940 North-Holland Publishing, Amsterdam, The Netherlands, 62-101, 1963.

941

942 Voortman, B. R., Bartholomeus, R. P., Van Bodegom, P. M., Gooren, H., Van Der Zee, S. E. A. T. M., and Witte, J. P. M.:
943 Unsaturated hydraulic properties of xerophilous mosses: towards implementation of moss covered soils in
944 hydrological models, *Hydrological Processes*, 2013.
945 Wallace, J. S., Lloyd, C. R., Roberts, J., and Shuttleworth, W. J.: A comparison of methods for estimating aerodynamic
946 resistance of heather (*Calluna vulgaris* (L.) Hull) in the field, *Agricultural and Forest Meteorology*, 32, 289-305,
947 [http://dx.doi.org/10.1016/0168-1923\(84\)90055-8](http://dx.doi.org/10.1016/0168-1923(84)90055-8), 1984.
948 Wouters, D. S., Keppens, H., and Impens, I.: Factors determining the longwave radiation exchange over natural
949 surfaces, *Arch. Met. Geoph. Biokl. B.*, 28, 63-71, 10.1007/bf02243835, 1980.
950 Yang, F., Mitchell, K., Hou, Y.-T., Dai, Y., Zeng, X., Wang, Z., and Liang, X.-Z.: Dependence of Land Surface Albedo on
951 Solar Zenith Angle: Observations and Model Parameterization, *Journal of Applied Meteorology and Climatology*, 47,
952 2963-2982, 10.1175/2008jamc1843.1, 2008.
953 Yin, Y., Wu, S., Zheng, D., and Yang, Q.: Radiation calibration of FAO56 Penman-Monteith model to estimate
954 reference crop evapotranspiration in China, *Agricultural Water Management*, 95, 77-84,
955 10.1016/j.agwat.2007.09.002, 2008.
956 Zhang, Y.-f., Wang, X.-p., Hu, R., Pan, Y.-x., and Zhang, H.: Variation of albedo to soil moisture for sand dunes and
957 biological soil crusts in arid desert ecosystems, *Environ Earth Sci*, 1-8, 10.1007/s12665-013-2532-7, 2013.
958 Zhou, M. C., Ishidaira, H., Hapuarachchi, H. P., Magome, J., Kiem, A. S., and Takeuchi, K.: Estimating potential
959 evapotranspiration using Shuttleworth-Wallace model and NOAA-AVHRR NDVI data to feed a distributed hydrological
960 model over the Mekong River basin, *J Hydrol*, 327, 151-173, 2006.
961 Zwolsman, J. J. G., and van Bokhoven, A. J.: Impact of summer droughts on water quality of the Rhine River - A
962 preview of climate change?, 56, 45-55, 2007.
963
964